A Low Gain Fine Mesh Photomultiplier Tube for Pure CsI

by

Derek Jun Fujimoto

B.Sc., McGill University, 2013

A THESIS SUBMITTED IN PARTIAL FULFILLMENT OF
THE REQUIREMENTS FOR THE DEGREE OF

MASTER OF SCIENCE

in

The Faculty of Graduate and Postdoctoral Studies

(Physics)

THE UNIVERSITY OF BRITISH COLUMBIA

(Vancouver)

October 2015

Abstract

The increased luminosity of the upgraded SuperKEKB accelerator in turn mandates an upgrade to the Belle detector. One proposed upgrade is to exchange the existing thallium doped cesium iodide scintillation crystals (CsI(Tl)) in the endcap calorimeter with pure cesium iodide (CsI). One advantage of pure CsI is its shorter decay time constant. This would reduce the amount of time taken to process each event, which in turn reduces the chance of simultaneously measuring the energy of different two particles (pileup). Hamamatsu Photonics has produced the R11283 photomultiplier tube with a nominal average gain of 255 ± 11, ideal for measuring the light produced by scintillation in pure CsI while in a magnetic field. A prototype array of 16 photomultiplier tubes was built and tested at TRIUMF. This work documents the characterization of the photomultiplier tube as well as University of Montreal's pre-amplification and shaper electronics. The primary results can be split into four distinct measurements: the electronic noise, the short term stability, the excess noise factor, and the lifetime. The electronic noise was initially measured with cosmic rays and was found to be (77 ± 2) keV using a Belle II pure CsI crystal. The short term stability was measured with a set of calibration sources, and the variation over a week was $(0.28 \pm 0.03)\%$ after temperature corrections. The excess noise factor was found to be $(1.9 \pm 0.1 \pm 0.4)$ using a pulsed UV laser. This result was accompanied by an additional electronic noise measurement of 1730 ± 33 electrons at the anode. The lifetime was found using a UV LED array and a ^{207}Bi source, with the gain $\times$ quantum efficiency reduced to $(93 \pm 3)\%$ after about 48 days of aging in real time. This was equivalent to 70 years of standard Belle II operation with 7 C having passed through the anode. There were several sets of aging behaviours observed, with some evidence that the anode charge is not the sole factor in aging.

Preface

While the motivation for the work presented is due to the Belle II Collaboration, my supervisor Christopher Hearty was responsible for most of the direction of the project, for dictating which measurements needed to be taken, and for providing a blueprint on how each measurement should be accomplished. He also provided support in the implementation of the setup. I was responsible for the implementation of his ideas, both in the setup and the analysis unless otherwise indicated. A lot of the work done in chapter 3 was prefaced by Chris and Eddie Ji [1][2].

Chelsea Dunning procured and light-proofed the dark box that was used in all measurements, as well as the incubator. She also helped with some of the setup in chapter 4, where she determined the best desiccant, helped prepare the incubator, and provided instructions for mixing the silicon rubber used in chapter 6. Pierre Amaudruz of TRIUMF put together the initial MIDAS readout and helped debug issues with the CAMAC crate. He was also responsible for building the pulsed UV laser, and provided the optics used in chapter 6. Jean-Pierre Martin and Nikolas Starinski of the Université de Montréal designed and built both versions of the preamp, the shapers, motherboards, and a high voltage divider. Version 4 of the preamp, and the shapers were only used in chapter 7, and the V3 preamp was used in the preceding chapters. The mixing of the silicone rubber and the gluing of the CsI pucks to the PPs was done with the aid of Dylan Jow. Many of the detector facility staff helped with the procurement of materials, as well as with suggestions for setup design. Notable persons include Wayne Faszer, Philip Lu, Peter Vincent, and Robert Openshaw. I designed and constructed all of the specialized setup pieces: the support structures for the excess noise measurement, the array support structure for the aging measurement, and modifications to the incubator and the dark box. With Chris' direction, I designed and implemented all of the circuits used in the presented work, with the exception of that in chapter 3.

All of the analysis was performed in C++ using the ROOT framework, developed at CERN. Many of the modifications to the MIDAS and ROOTANA readout code were also implemented by me, in particular for

the measurements after, and including, chapter 6.

Table of Contents

Appendices

List of Tables

List of Figures

Acknowledgements

I would like to extend my thanks to my supervisor, Christopher Hearty, for his guidance and instruction. Additionally, in recognition of their support and advice: my fellow students and friends, with particular acknowledgement to Alon Hershenhorn for idea brainstorming and enforced coffee/tea breaks, as well as Jean-François Caron for his useful insights into ROOT and C++. The TRIUMF support staff have also earned my gratitude for their help in DAQ and setup, in particular: Wayne Faszer, Philip Lu, Peter Vincent, Robert Openshaw, and Pierre Amaudruz. Lastly, for their continued support, my parents.

Chapter 1

Introduction

1.1 Belle Physics

The concept of the atom has existed since the time of ancient Greece, but only recently has the field of subatomic particle physics emerged. One of the first in this field was Rutherford's gold foil experiment [3]. He showed that the atom was composed of at least two separate entities: the nucleus and the electron. Since then, particle physicists have worked to find the complete set of fundamental particles and to refine the laws that govern their interactions: the standard model.

In their quest for new physics, modern particle physics experiments have two primary strategies: direct searches and indirect searches. While both make use of particle colliders, direct searches for new physics focus on the production of new forms of matter by increasing the collision energy. In contrast, indirect searches focus on the observation of extremely rare processes where deviations from the expected proportions of collision products can be traceable to new physics in the underlying mechanism. The indirect searches for new physics are often termed flavour physics, as they are the careful study of the interactions and combinations of each species, or flavour, of particle.

The KEK B-factory is an asymmetric e^+e^- collider situated in Tsukuba, Japan [4], with the goal of producing a large number of B mesons for the study of flavour physics. The detector at the KEKB interaction point, Belle, was designed in particular to observe CP violation in B mesons [5], and from 1999 to 2009 the Belle detector acquired an integrated luminosity of 1000 fb^{-1} [6]. While most of this data set was at the $\Upsilon(4S)$ resonance, the ideal location to produce $B\bar{B}$ pairs vital to the study of B mesons, Belle was also able to provide a series of unique data sets on other Υ resonances [5]. In addition to increasing the precision of many standard model parameters, Belle, together with its sister experiment BABAR [7] at SLAC, provided evidence of CP violation in 2001 [8][9] resulting in the 2008 Nobel Prize for physics and the theory of CP violation [10].

The next generation of high luminosity machines will again push the

boundaries of known physics. The next iteration of the KEKB accelerator, SuperKEKB, will be well positioned to study energy scales beyond those attainable by current generation direct search programs. For example, flavour-changing neutral-current processes are known to be particularly sensitive to new physics which does not have the same suppression mechanisms as is present the standard model [11]. A high luminosity experiment studying phenomenon of this type will therefore be sensitive to the same mechanisms, even if these mechanisms deviate from the standard model at extremely large energy scales.

The SuperKEKB asymmetric e^+e^- collider has a luminosity goal of $8 \times 10^{35} cm^{-2} s^{-1}$ [6], a factor of 40 increase over the luminosity achieved by KEKB. SuperKEKB uses the same beam pipe as KEKB (other than at the interaction point) and the corresponding upgrade to Belle, Belle II, will make use of the existing Belle structure. The increased luminosity presents many challenges for Belle II. Relevant to this body of work are the pileup in, and the irradiation of the endcap calorimeter (endcap ECL). It is estimated that the background rates in the ECL will be a factor of twenty larger with the increased luminosity [12]. Despite the continued performance of the Belle scintillation crystals [13], it was proposed by the collaboration that the thallium-doped cesium iodide (CsI(Tl)) scintillation crystals should be replaced with pure CsI [6]. Pileup occurs when two or more particles interact with the crystal within the crystal's decay time. In this case the energy of the two particles is additive, resulting in a much larger signal than would otherwise result. Pure CsI has a much shorter scintillation time constant than CsI(Tl) [14][15][16] which will help reduce the number of pileup events, important for missing energy studies [6].

1.2 The Belle II Endcap Calorimeter

As seen in figure 1.1, the endcap calorimeter is located at either end of the barrel section. The main tasks assigned to the endcap ECL are: the detection and determination of photon energy and angular coordinates, electron identification, trigger generation, luminosity measurement, and to assist in K_L^0 detection [6].

The Belle endcap ECL contained 8736 CsI(Tl) crystals, weighing a total of 43 tons, each a truncated pyramid in a variety of proportions to cover 91% of the total 4π solid angle [18]. Each crystal has a cross section of about 5.5 cm $\times$ 5.5 cm and a length of 30 cm. Each was wrapped in a Gore-Tex film layer and an aluminized mylar layer [13]. The optical readout

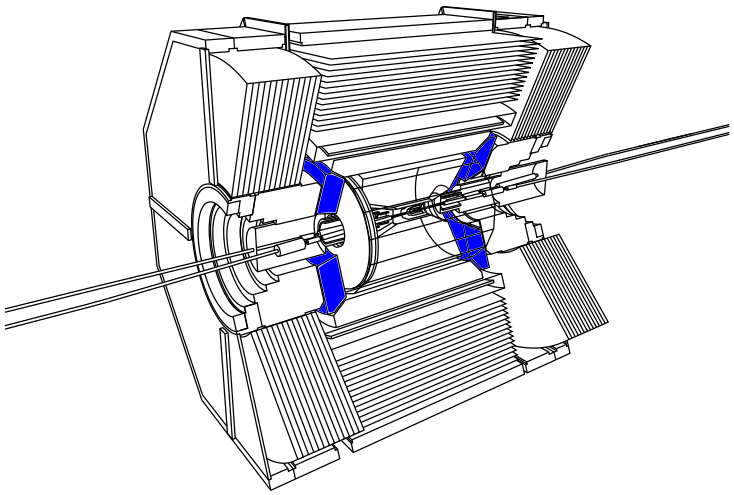

Figure 1.1: *Belle II detector with endcap ECL highlighted [17].*

was performed by two PIN photodiodes, each with its own preamp directly mounted to the crystal [18]. Over the course of four years of operation, the cumulative dose in the endcap scintillation crystals was about 100 rad. With the radiation levels expected increase by a factor of 20 for SuperKEKB, it is expected that the light output of the CsI(Tl) will decrease by about 25% [18]. Although this is not a pressing concern, the pile up noise due to the increased particle rate and the slow scintillation time of CsI(Tl) pose a more serious problem. Therefore, major improvements could be made to the endcap ECl by replacing the existing CsI(Tl) in the endcaps with a faster version of the crystal.

The Belle II Technical Report details three options for the upgrade to the endcap calorimetry [6]:

- Pure CsI crystals with a photomultiplier tube readout.
- A lead tungstate crystal, dubbed PWO-II by the PANDA experiment [19], with an avalanche photodiode (APD) readout.
- $Bi_4Si_3O_{12}$ crystals with APD readout.

The most promising option at this time is the pure CsI, due to its moderate cost, good performance, and ease of production. The proposal for the

pure CsI option was to keep the existing Belle support structure and barrel CsI(Tl) crystals, but to replace the endcap crystals with pure CsI and upgrade all readout electronics [20].

A large part of the Canadian contribution has been to the research of the pure CsI option. CsI has two components to its scintillation time constant: a fast component of about 30 ns [16], and a slow component of about 1μs [14]. This is in comparison to CsI(Tl) which has a one component time constant of 1μs [15]. It should be noted, however, that the light output of pure CsI is about one tenth of CsI(Tl) [6]. To keep the equivalent noise energy at the level obtained during the Belle experiment, the PIN photodiodes will have to be replaced with the aforementioned photomultiplier tube readout, as the noise to signal ratio is lower. Additionally, the PIN diodes are not sensitive to UV, making the photopentodes are better suited to read out the spectrum of pure CsI.

The work presented is an examination of a proposed photomultiplier tube for use with the pure CsI option. All of the measurements were carried out in the detector facility at TRIUMF and share some basic features: the photomultiplier tube was kept in a dark box, which was grounded to reduce pickup and noise levels. Also, the temperature and humidity of the box was continually recorded, and the humidity was controlled with a desiccant. This was to reduce damage to the surface of the slightly hydroscopic CsI.

Chapter 2

The Low Gain Fine Mesh Photopentode

2.1 On the Operation of Photomultiplier Tubes

A photomultiplier tube (PMT) is a device for detecting low levels of light, and in some cases, single photons. As seen in figure 2.1, a PMT has three primary components: the photocathode, the anode, and the dynodes.

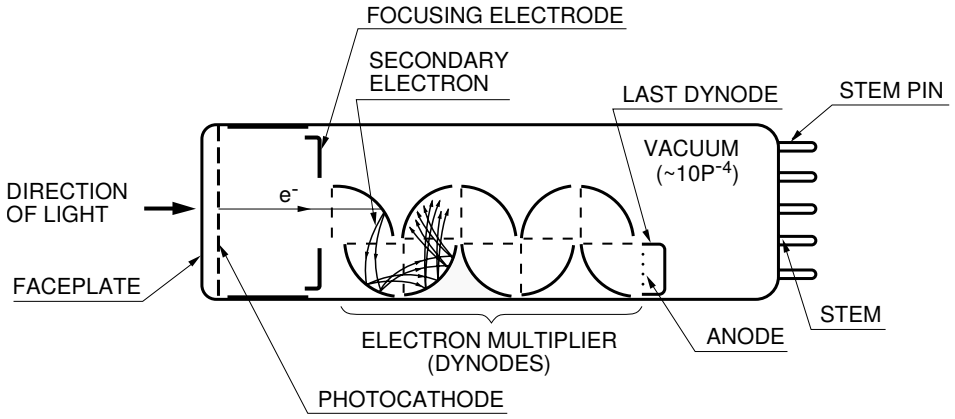

Figure 2.1: *The electron multiplication process in a PMT [21].*

The photocathode converts a single photon into a single electron with some probability (the quantum efficiency). The photocathode is a semiconductor and can be described using a band model. Electrons in the valence band of the photocathode can absorb energy from an incident electron and become excited. With enough photon energy, the election is emitted from the material and is free to propagate. Electrons emitted from the photocathode are called the photoelectrons and are guided towards the dynodes by means of an electric field and careful dynode placement [21].

The dynodes are the portion of the PMT that multiply the electrons

into a signal that is readily measurable. For every electron incident on each dynode, an average of $\delta > 1$ secondary electrons are ejected. The following cascade of electrons results in the multiplication of the original signal. The dynode collection efficiency is determined by the material and the geometry of the dynode, while the secondary emission ratio (δ) is a function of the voltage applied to the dynode and the dynode material.

The anode of the PMT is the final stage of the electron multiplication process. It collects the electrons after the dynode cascades and outputs the electron current, which is measured. In this way, the charge at the anode is proportional to the amount of light incident on the PMT.

The gain of the PMT is the factor by which the number of photoelectrons has been multiplied at the anode. High sensitivity PMTs can have 19 dynode stages with gains on the order of 10^6.

2.2 The R11283 Photopentode

Hamamatsu Photonics has produced a PMT that closely matches the specifications outlined in the Belle II Technical Report [6]. This PMT has five flying leads to power the dynodes and to read out the current from the anode. Because of the five leads, this PMT has been given the nickname "photopentode" (PP) by the collaboration. The PP (model R11283) has three fine mesh dynodes (fig. 2.2) which allows it to have a high immunity to magnetic fields. This is because the dynodes can be placed in close proximity to each other, reducing the path length between dynodes. Unlike more typical PMTs whose dynodes are solid plates, the fine mesh has a poor electron collection efficiency and electrons can bypass a dynode entirely, contributing to the noise of the signal. The factor by which this process increases the square of the resolution is called the excess noise factor (F). The measurement of the excess noise factor is described in chapter 6. The R11283 PP has a UV transparent, 2 inch diameter window, closely matching the size of the CsI crystals in the Belle ECL. In particular, the PP is responsive to light with wavelengths from 185 nm to 650 nm, with maximal response at 420 nm [22]. This makes it ideal for recording the output of pure CsI, as the maximum of the emitted

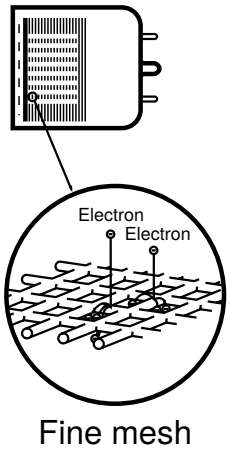

Figure 2.2: *The fine mesh dynode [21].*

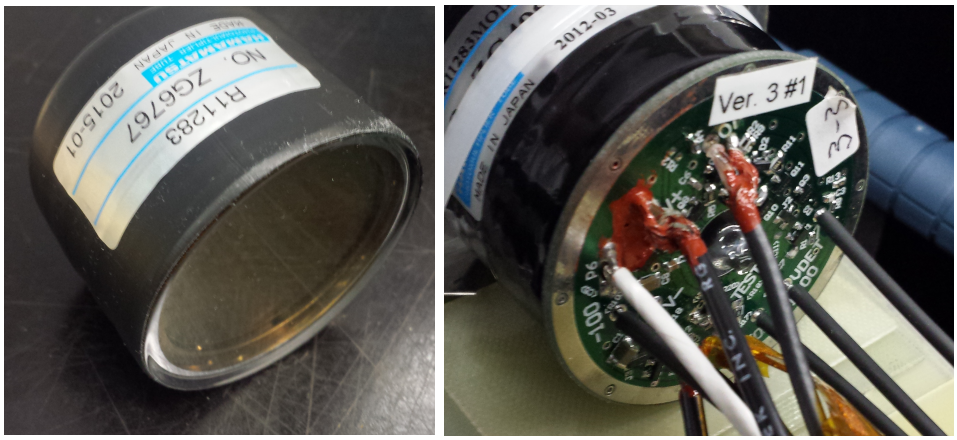

(a) *Window (photocathode) side.* (b) *Rear (anode) side, with preamp.*

Figure 2.3: *The Hamamatsu R11283 photopentode with version three of the Université de Montréal preamp (right).*

light spectrum of the material is 315 nm [14]. R11283 is a head-on type, with a bialkai photocathode and a typical gain of 255 ± 11 (ch. 5) at the maximum operating voltage of -1000V. The low gain of the PP is to ensure that the current at the anode does not exceed the voltage divider's specifications. If the gain is too large, then the dynodes draw too much current during the multiplication process and the PP does not perform as expected.

The version of the PP used required the assembly of a custom voltage divider, preamp, and shaper electronics. The voltage divider's purpose is to take a single input voltage and redistribute it among the dynodes. The preamp and the shaper together produce a signal whose amplitude is proportional to the amount of charge passing through the anode. These electronics were designed and produced at the Université de Montréal [23]. Version 3 of the Montréal preamp can be seen in figure 2.3, attached to the R11283 PP (appendix B.1.1). The preamp is situated directly on the flying leads of the PP and the preamp signal is sent to the shaper which can be off site, allowing for reduced space requirements in the detector ECL.

In addition to the above characteristics, the R11283 is an ideal PMT for the Belle II ECL because of its relatively low cost when compared to other PMTs with similar properties.

Chapter 3

Electronic Noise

3.1 Introduction

The electronic noise was an important first quantity to measure since it dictated whether or not low energy measurements would be viable. This source of random uncertainty is due to the processing electronics, namely the preamp and the shaper. The primary goal of this measurement was to find the equivalent noise energy (ENE). This is the electronic noise in units of energy deposited in the CsI crystal. In this way, the effect of the electronics on the energy resolution is comparable. The ENE was measured using cosmic muons.

3.2 Experimental Setup

As with all of the measurements presented in this work, the experimental setup was encased in a light-tight box (appendix B.3.1) which provided a low light environment for the phototubes, restricted air flow so that the interior could be kept at a low humidity, and shielded the setup from pickup. A molecular sieve desiccant (appendix B.3.2) was used to keep the humidity to about 10% relative humidity within the dark box.

Two plastic scintillators with standard PMTs were used to generate a trigger which selected for cosmic muons. As seen in figure 3.1, any cosmic particle which generates a trigger has to travel first through the top plastic scintillator, then through the CsI, the lead bricks, and finally the bottom plastic scintillator. Requiring the coincidence of the two plastic scintillators ensures that the particle was a minimum ionizing muon which travelled through the CsI, since the lead prevents all other particles of lower momentum from reaching the second scintillator.

The CsI crystal used was on loan from the Budker Institute of Nuclear Physics (BINP) and is of the same size and style as a Belle II endcap ECL crystal (appendix B.3.3). The PP was connected to the crystal via an optical grease produced by Saint-Gobain (appendix B.2.1). The setup in the dark

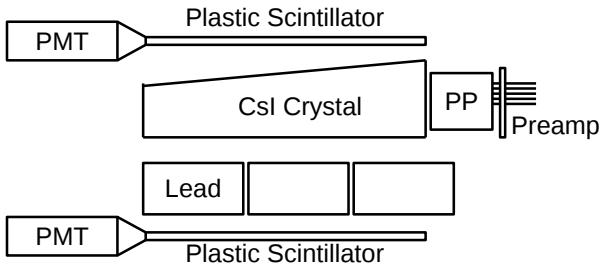

Figure 3.1: *Experimental setup (side view). Coincidence on the plastic scintillators provide the trigger and lead shielding ensures that the cosmic particle is a minimum ionizing muon.*

box can be seen in figure 3.2.

The PP output from the anode was first processed by the V3 preamp. The signal was then sent to an Ortec 474 Timing Filter Amp which served as the shaper, and the output waveform was recorded by a Teledyne LeCroy WavePro 740Zi oscilloscope. The Ortec shaper had an integration and differentiation time constant of 50 ns. Refer to figure A.1 for circuit minutiae.

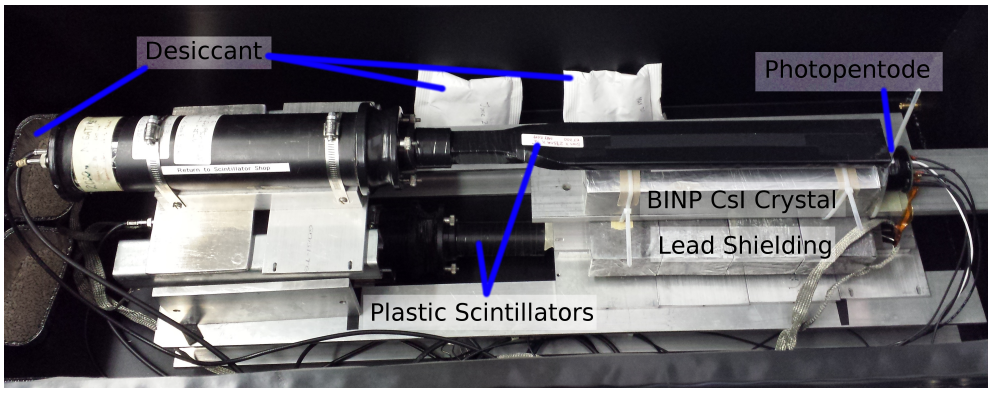

Figure 3.2: *Experimental setup. Two plastic scintillators were used on top and on bottom of the CsI crystal for the cosmic muon trigger.*

3.3 Results and Analysis

3.3.1 The Electronic Noise and the ENE

Due to the limitations of the scope's dynamic range, the electronic noise was not measurable directly. At the scales necessary to capture the full signal waveform, the uncertainty of each bin was dominated by the scope uncertainty, whereas the electronic noise could only be resolvable without the muon signal present. The plan was therefore:

- Record signal waveforms: a cosmic muon had deposited energy in the CsI.
- Find the average signal waveform.
- Record empty waveforms: no energy was deposited in the CsI.
- Construct a probability distribution function (PDF) from the average waveform.
- Construct combined waveforms: the sum of the empty waveforms and the average waveform.
- Fit the PDF to the combined waveforms and observe how the empty waveforms affect the fit parameters.

A typical cosmic muon event can be seen in figure 3.3. About 5500 of these events were collected over the course of about 15 hours.

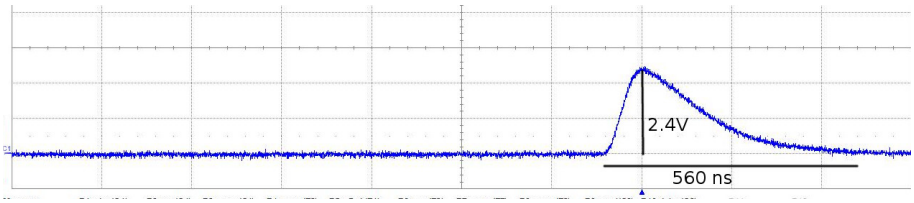

Figure 3.3: *Screenshot of a cosmic muon event (shaper output) in the CsI crystal from the oscilloscope. Pulse height: ≈2.4 V, pulse length: ≈560 ns.*

A portion of these were not useful, either because the events were empty or because the event energy was so large that the oscilloscope range was exceeded. Figure 3.4 shows the distribution of the maximum value of the 5500 signal waveforms. It should be noted that the oscilloscope set an artificial offset to all of the voltage values, to make better use of the oscilloscope's range. This did not affect the outcome as a pedestal was established by recording a large portion of the waveform prior to the trigger. Waveforms with maximum values peaking at -5.8 V had no evidence of a cosmic muon,

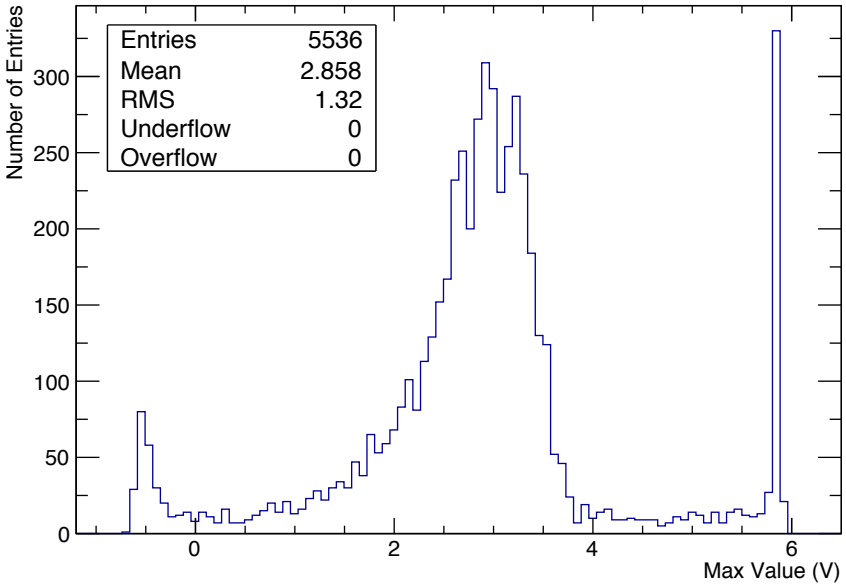

Figure 3.4: *The distribution of the signal waveform maximum values. This was used to discriminate against empty events or PP over-saturation. Events in the range of [-4,0] V survived the cut.*

whereas waveforms with maximum values near 0.5V had surpassed the range of the scope. The values kept were events with maximum values within the range of $[-4, 0]$ V, with 84% of the events surviving the cut.

The signal waveforms were then averaged bin-by-bin, with the result seen in figure 3.5. This average waveform eliminated all significant variability from the signal, including the variability due to the energy deposited in the CsI by cosmic muons. The noise from the electronics was then re-introduced in the combined waveforms.

The normalized PDF used in the fits had three parameters: the height (a scaling factor), the pedestal (a voltage offset), and a time offset. A typical signal waveform with PDF fit can be seen in figure 3.6. The height of the PDF is proportional to the energy deposited in the CsI crystal.

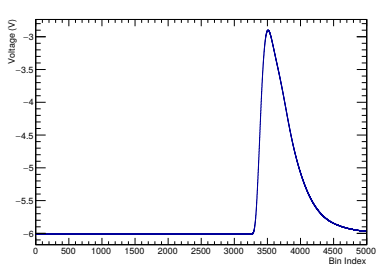

Figure 3.5: *The average signal waveform after the cut. This was then normalized to have a height of one to make the PDF. Each bin corresponds to 0.4 ns.*

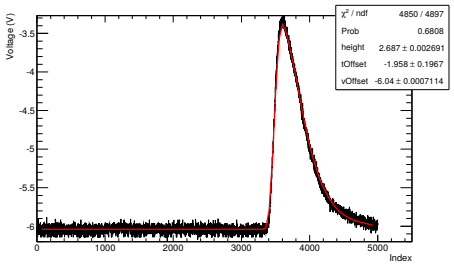

Figure 3.6: *The PDF generated from figure 3.5 fitted to a typical signal event.*

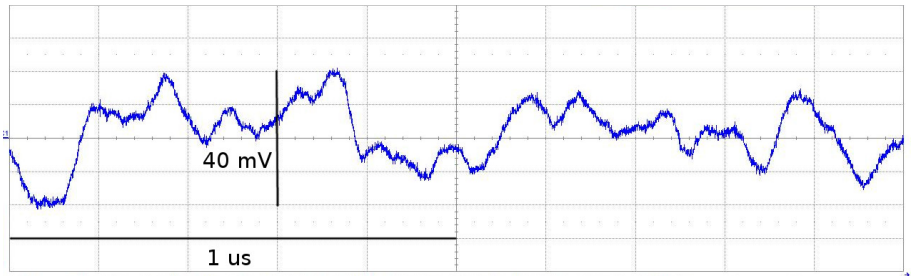

Figure 3.7: *Screenshot of a empty event (no cosmic event) from the oscilloscope. Waveforms such as this one were added bin-by-bin to the average waveform in figure 3.5.*

An example of an empty waveform can be seen in figure 3.7. Events such as these were added bin-by-bin to the average waveform from figure 3.5. The fits to these sums were then affected by the electronic noise, while the variation in muon energy was eliminated. The distribution of the fit heights to the combined waveforms can be seen in figure 3.8, and the width of this distribution was the electronic noise: (5.89 ± 0.08) mV.

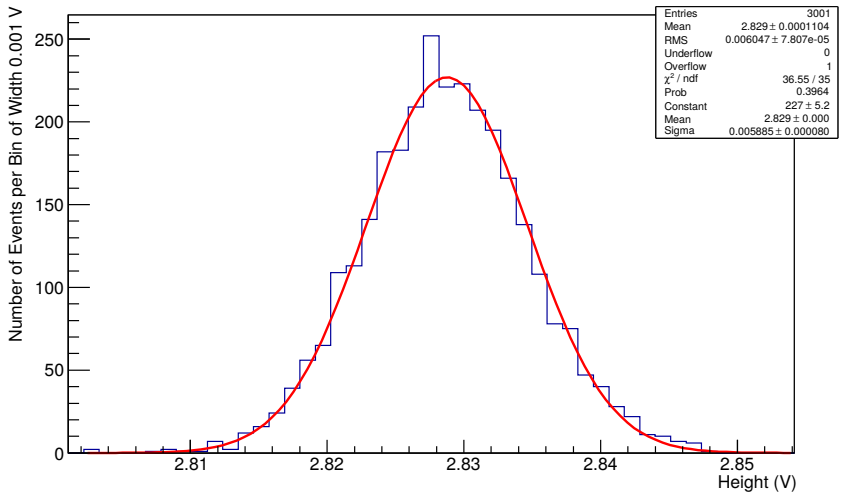

Figure 3.8: *The distribution of heights of the fit of the PDF to the noise + average waveform with Gaussian fit. The standard deviation of the distribution was* (5.89 ± 0.08) *mV.*

This value needed to be converted into units of energy. To do so, the signal waveforms were fitted with the PDF (fig. 3.6) and the peak heights were histogrammed, as seen in figure 3.9. Since the distribution is bounded by zero, it cannot be accurately described with a Gaussian. The fitted function used was an asymmetric Gaussian, dubbed the Novosibirsk function by the collaboration. The Novosibirsk function is the convolution of a log-normal distribution and the theoretical energy spectrum due to Compton scattering (appendix C.1).

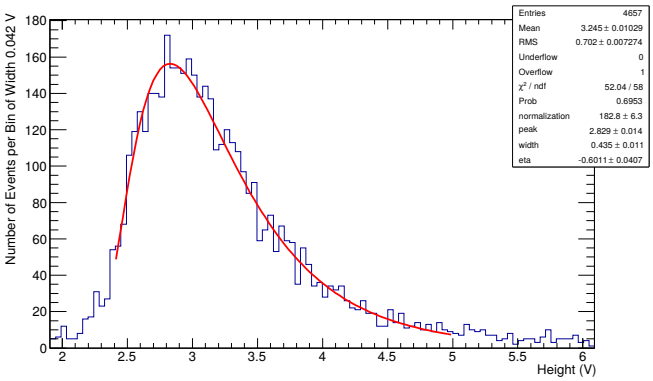

Figure 3.9: *The distribution of the heights from fitting the PDF to the signal events. This was used to convert the standard deviation in figure 3.8 into units of energy.*

Given that the most likely energy deposit due to a muon along the 30 cm length of the CsI crystal is 190 MeV[24], and that the average crystal height was 5.88 cm, the most likely energy deposit in the CsI due to a cosmic muon travelling along the vertical axis was about 37.2 MeV. This energy value corresponds to the peak of the distribution of the signal peak heights (fig. 3.9). The conversion rate from the electronic signal to units of energy was (13.16 ± 0.07) MeV/V. Applying this to the standard deviation of the distribution of the heights of the combined waveforms (fig. 3.8), the ENE was found to be (77 ± 2) keV.

3.3.2 The Other Fit Parameters (Signal Waveform Fits)

It was also instructive to consider the distributions of the other fit parameters. Figures 3.10 and 3.11 respectively show the distribution of the pedestals and the time offsets from fits to the signal waveforms. In both, there is evidence of a bimodal structure. The distribution of the pedestals was likely due to pickup, and would be a constant factor throughout the entire signal waveform. This would be corrected for by the pedestal fit parameter.

To investigate if the distribution of the time offsets was an artifact of the fitting, the leading edge of the signal waveform was fitted with a linear line (fig. 3.12). The distribution of the intersect of the fit and the average pedestal also produced the bimodal features seen in figure 3.11. Additionally, adding a delay to the signal from either the top or bottom plastic scintillators did not remove this effect. Rather, with the lower scintillator delayed, the

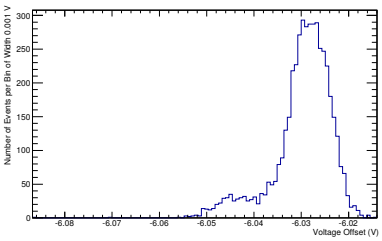

Figure 3.10: *The distribution of the pedestals from fitting the PDF to signal events.*

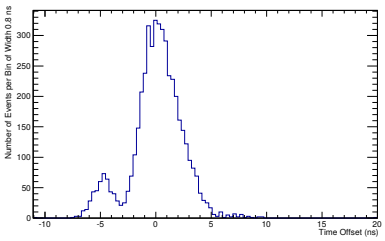

Figure 3.11: *The distribution of the time offset from fitting the PDF to signal events.*

bimodal distribution from figure 3.11 resulted, whereas if the upper counter was delayed, the time offset distribution had three, well-separated peaks. This pattern was repeated when a standard PMT was used to read out the crystal. It was therefore concluded that the bimodal distribution of the time offset arose from the timing of the plastic scintillator counters and not the CsI or PP system. See appendix D.1 for a comparison of the time offset distributions from this analysis.

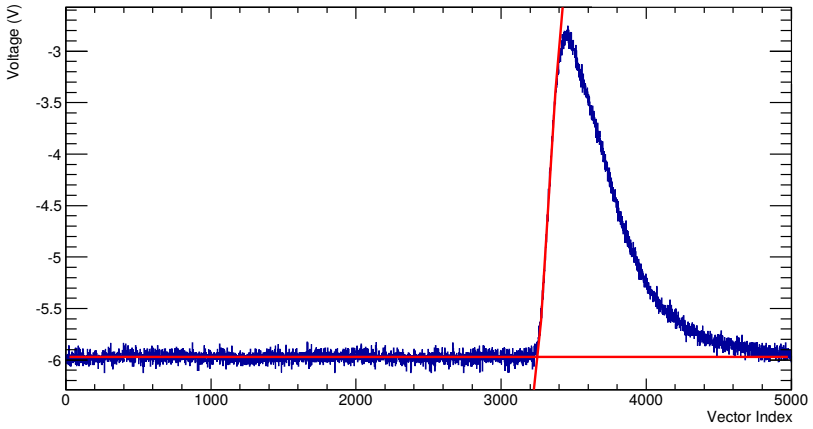

Figure 3.12: *Checking the fitting of the PDF to the signal waveforms. The bimodal peak structure in figure 3.11 was still present. Each bin represents* 0.4 *ns.*

3.3.3 The Other Fit Parameters (Combined Waveform Fits)

It was seen that the signal height and voltage offset from the fits to the combined waveforms were correlated. To compare, a set of randomly generated noise data was added to the averaged waveform and was fitted with the PDF. The lack of a correlation in this case (fig. 3.13), illustrates an issue with the fitting of the combined waveforms. Since the shaper takes a signal that approximates a delta function and stretches it into a full waveform, it was thought that the bins of the measured noise waveforms would contain overlap from neighbouring bins and would not be fully independent. This would be in violation of one of the base assumptions in the minimization package provided by ROOT. To do this properly, the chi-squared would have to be calculated and minimized using the full covariance matrix.

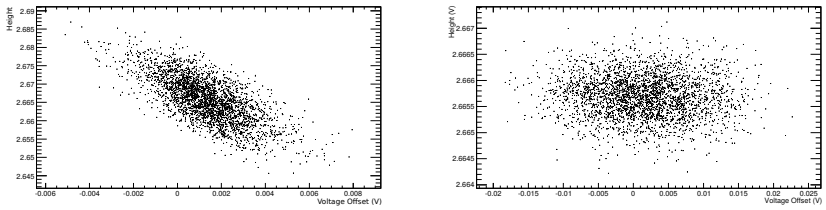

(a) *Real noise correlation.* (b) *Fake noise correlation.*

Figure 3.13: *Voltage offset correlation comparison for both measured and generated noise added to the averaged signal waveform. It was noted that only the combined waveform with the measured noise set was correlated.*

3.4 Conclusion

It was tentatively concluded that the equivalent noise energy of the R11283 photopentode, using the Belle II pure CsI crystal from BINP and the Université de Montréal preamp, was (77 ± 2) keV for 37.2 MeV cosmic muons. The result was tempered by the correlation found between two of the fit parameters of the fits to the combined noise signals, which suggest that there was a violation of the assumption that the bins in the noise signal were independent. To properly follow this study, the covariance matrix of the waveforms would have to be constructed and from this the chi-squared can be calculated and minimized. The ENE was also found in chapter 6 using a different methodology and a smaller, high quality CsI crystal.

Chapter 4

Short Term Stability

4.1 Introduction

The goal of this measurement was to find the variability in the photopentode and electronics output after correcting for variations in temperature. In contrast to the electronic noise measurement of chapter 3, a light source of reproducible intensity was needed. This was provided by the scintillation of gamma rays in a small CsI crystal. The gamma rays were emitted by one of three calibration sources, and the stability over a week was determined from the signal produced by the CsI crystal. By virtue of using calibration sources with known decays, the linearity of the PP signal with energy was also observed.

4.2 Experimental Setup

As mentioned in the introduction, this measurement used a calibration source to provide gamma rays to induce scintillation in the CsI crystal. The crystal was procured from Saint-Gobain and was much smaller than the BINP Belle II crystal: a cylinder of 2.7 cm in diameter and 2.5 cm in length. The small crystal size reduced the number of cosmic events, as well as to increase the efficiency with respect to the amount of light collected by the photopentode (PP). To increase the data collection rate, a peak finding analog to digital converter (ADC - appendix B.1.4) was used in the place of the oscilloscope. The data acquisition (DAQ) software was handled by the MIDAS framework [25]. The use of the calibration sources also permitted the correlation of the ADC readout to the amount of energy deposited in the crystal. Figure 4.1 shows a drawing of the setup. An acrylic puck was used

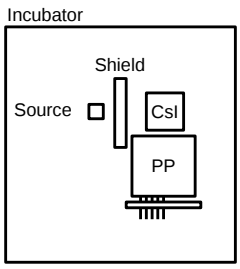

Figure 4.1: *Setup to measure the short term stability of the PP, top-down view.*

to shield the crystal from any beta radiation from the calibration source. The whole setup was encased in an incubator (appendix B.3.5) to control the temperature as much as possible. The temperature was measured to be $(34.5 \pm 3)\ ^{\circ}C$ over the course of the measurement. The incubator was placed within the same dark box as was used for the electronic noise measurement. A hole was cut in the corner of the incubator window to let cables pass through, and any gaps were plugged with foam. Figure 4.2 shows the setup

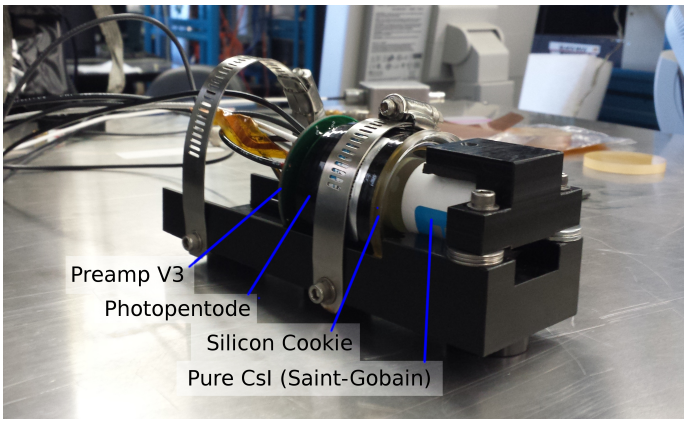

Figure 4.2: *Device for holding the PP and CsI crystal in place. The optical connection pictured is a rubber silicon cookie, but the measurements used an air gap since it was more reproducible.*

that was encased in the incubator. While the pictured setup makes use of a silicon cookie for the optical conduit, an air gap was used in the final measurement. The air gap was preferred over both the optical grease used in chapter 3 and the cookie because of the reproducibility of the measurement. The cookie had a tendency to detach from the crystal or the glass of the phototube, or to trap air pockets when applied. Both cases left the optical conductivity non-uniform across the surface of the PP. With the optical grease, the amount of grease applied affected the output, and the grease reacted with the CsI, yellowing it with time. Of the three, variations in the air gap produced the least variation in output. The air gap was maintained to less than a millimetre for the experiment, but the size of the gap was not precisely controlled.

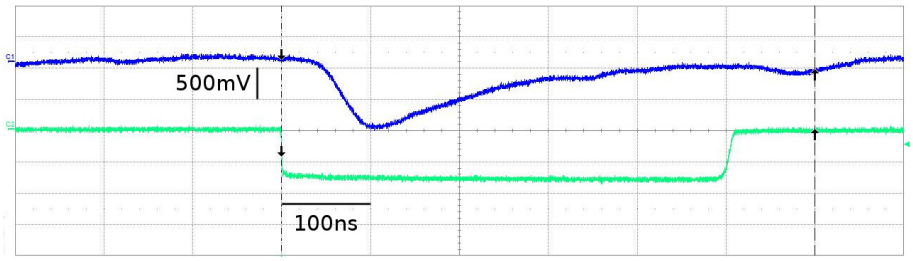

Figure 4.3: *Screenshot of the waveform output of the Ortec 474 shaper, with the NIM gate used to trigger the ADC. The gate generation was based on a discriminator threshold set on the shaper output.*

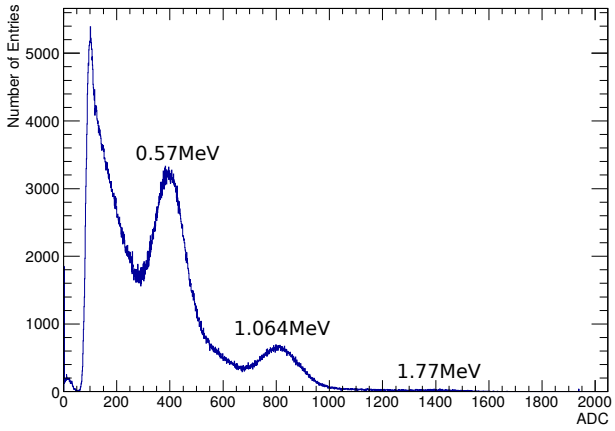

Figure 4.4: ^{207}*Bi spectrum as seen by the ADC using the described setup. There are three peaks for* ^{207}*Bi but one of them has very low statistics. The cutoff at about bin 75 is the location of the discriminator threshold, and the small peak below that is due to a random trigger.*

Three calibration sources were used to generate signals: ^{22}Na, ^{137}Cs, and ^{207}Bi (appendix B.3.6). The shaper output was amplified to put the output peak heights near the center of the range of the peak-sensing ADC used to digitize the signal (appendix B.1.4). After amplification, the signal was split: one copy was sent to the ADC and the other to a discriminator used to produce the gate. The full circuit can be found in figure A.2 in the appendix. A signal from the amplifier and the corresponding gate can be seen in figure 4.3.

The DAQ software used to process the ADC signals was the MIDAS and

ROOTANA frameworks [25], which were written at TRIUMF (Canada) and PSI (Switzerland). The distributions of the ^{207}Bi peak heights as measured by the ADC and recorded by MIDAS can be seen in figure 4.4. Since the peak sensing ADC had a DC offset, the initial plan was to use a random trigger and to determine the pedestal from the peak produced by noise readings. This is the small peak below the discriminator threshold in figure 4.4. As seen in appendix B.1.4, the L2259B ADC is non-linear for small inputs and the pedestals were instead determined from plotting the decay energy against the ADC peak location.

4.3 Results

Due to backscatter, the spectra from the various calibration sources contain a background that was roughly exponential in nature, whereas the peaks themselves could be described with a Novosibirsk function. Figure 4.5 shows a fit of the sum of a Novosibirsk function and an exponential to the peak of the ^{137}Cs source. The peak location of the Novosibirsk fit was the value used for the PP response.

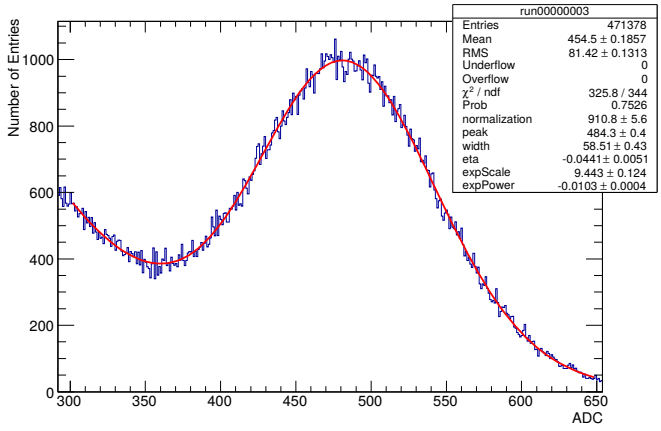

Figure 4.5: ^{137}*Cs spectrum (zoomed in on peak) fitted with the sum of a Novosibirsk function and an exponential. The peak of the Novosibirsk function was used to track the PP response.*

This was done with all three of the calibration sources to determine the linearity of the PP with respect to the energy deposited in the CsI. The analysis also resulted in the conversion rate from ADC bin to energy, and

the pedestal of the ADC for the linear region. The result can be seen in figure 4.6. The intercept of the linear fit was used as the pedestal the the following chapters, and was subtracted from the peak locations. The slope is the ADC bin to energy conversion rate.

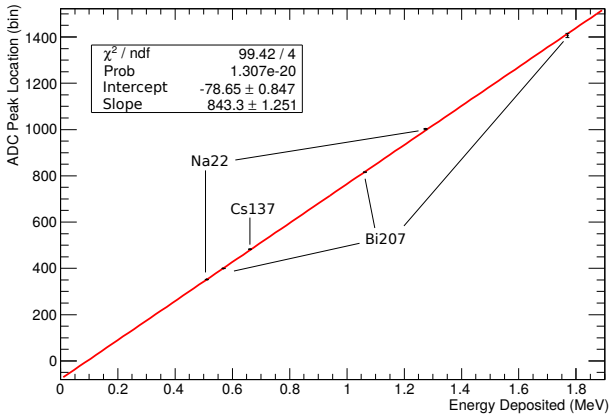

Figure 4.6: *ADC response as a function of energy deposited in the Saint-Gobain pure CsI crystal. The response is linear. See figure D.2 in the appendix for the residuals from the fit.*

For the short term stability, only the ^{137}Cs source was used. This was because a consistent light source was needed, so only one decay was required, and the lack of additional decay energies meant that the location of the ^{137}Cs peak was not affected by backscatter from other decay energies. The PP peak height spectrum was histogrammed for about a week, with each histogram covering one hour. Temperature measurements were made every 15 minutes. It is worth noting that the precision of the temperature reader (appendix B.3.4) was only 0.1 $^{\circ}C$. The peak location of the ^{137}Cs source with the temperature overlay can be seen in figure 4.7, with an obvious correlation between the two measurements. Figure 4.8 shows the correlation directly. In both, there is evidence that the first 8 to 12 hours of measurements do not correlate with temperature. It is thought that since the interior of the PP is a vacuum, the rate at which the dynodes equilibrate to the temperature is very slow. The response of the CsI crystal itself does vary with temperature [14][16], but this only accounts for about half of the variation observed, the total of which was $(-1.65 \pm 0.02)\%/^{\circ}C$.

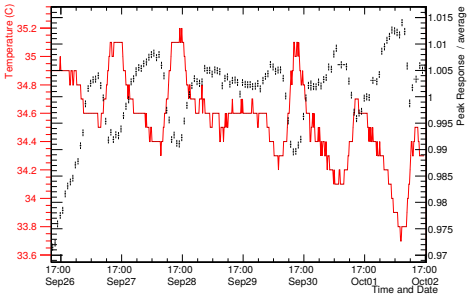

Figure 4.7: *CsI peak response with temperature overlay using the ^{137}Cs as the source of gamma radiation. Note that there appears to be a stabilization period of about 8-12h.*

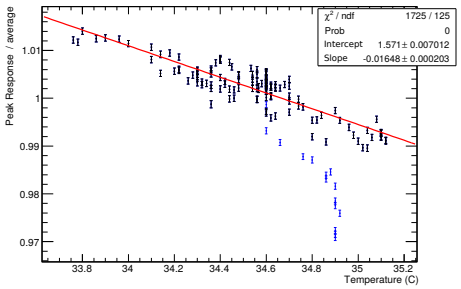

Figure 4.8: *CsI peak response as a function of temperature. The points in blue mark the period over which the PP was stabilizing. The temperature sensitivity of the combined setup was found to be* $(-1.65 \pm 0.02)\%/^{\circ}C$.

Given the temperature correlation, it was then possible to correct the peak locations in figure 4.7 to eliminate effects due to a variation in temperature. The temperature independent peak response can be seen in figure 4.9. It seen that the stabilization period still exists, and that the variation in peak location has decreased. Figure 4.10 shows a histogram of the peak response, with a Gaussian fit to determine the variability in the response after corrections to temperature. This residual instability was found to be $(0.28 \pm 0.03)\%$.

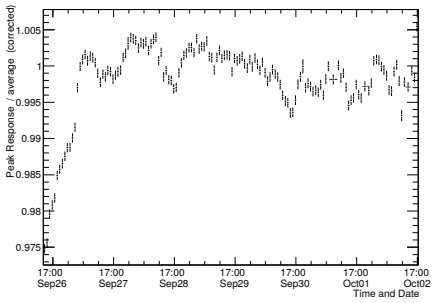

Figure 4.9: *The peak response in figure 4.7 corrected for temperature.*

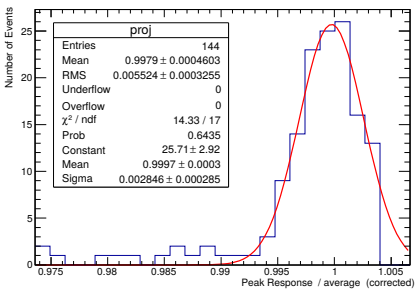

Figure 4.10: *A projection of the peak response of the temperature corrected points in figure 4.9. The variability after temperature corrections was* $(0.28 \pm 0.03)\%$.

4.4 Conclusion

Using a variety of radioactive calibration sources, it was found that the response of the PP to energy deposited in the pure CsI crystal is linear. Gamma rays from a ^{137}Cs source were used to track the peak response of the system over the course of a week. Despite the use of the incubator, some temperature variation was observed with a corresponding change in the peak location. This change amounted to $(-1.65 \pm 0.02)\%/^{\circ}C$ and is significantly larger than the variation of the CsI itself. After correcting for the temperature variation, the residual variability of the response was $(0.28 \pm 0.03)\%$ from the average.

Chapter 5

Hamamatsu Measurements

5.1 Introduction

Sixteen photopentodes (PP) were acquired from Hamamatsu, who provided a data sheet specifying several measurements performed before shipping. These measurements were the cathode luminous sensitivity (μA/lm), the anode luminous sensitivity (μA/lm), the dark current (nA), and the cathode blue sensitivity index. The cathode luminous sensitivity is proportional to the quantum efficiency of the cathode, whereas the anode sensitivity is proportional to the product of the gain and the quantum efficiency. The dark current is the current through the anode after 30 minutes sealed in a dark box, whereas the cathode blue sensitivity index is the cathode luminous sensitivity with a blue filter applied to the light source. All of the Hamamatsu measurements were carried out at an operating voltage of -750 V, and a Tungsten filament lamp was used as the light source. With these measurements and the 16 PP, the goals for this part of the experiment were to determine some of the tube-to-tube variation as well as to search for correlations between the Hamamatsu measurements and the ADC/energy slope of chapter 4 to set parameters for quality control.

The experimental setup for this chapter was unchanged from the short term stability, described in section 4.2.

5.2 Results

5.2.1 On the Hamamatsu Measured Values

Of the four measured values provided by Hamamatsu, the dark current was the least useful. The dark currents were measured to a precision of 0.01 nA, which was not good enough to properly get a sense of how well the PP were performing. The average dark current of the 16 PPs was (0.011 ± 0.007) nA.

The anode and cathode luminous sensitivity are both measures of the PP response to light. The distribution of each can be found in figure 5.1. It was seen that the cathode luminous sensitivities varied by 13% across the tubes,

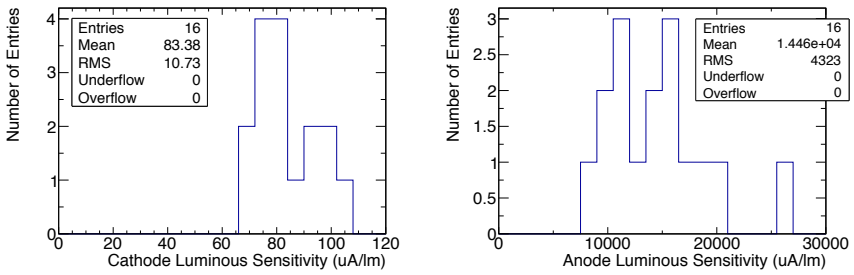

Figure 5.1: *Cathode and anode luminous sensitivities as measured by Hamamatsu at an operating voltage of* -750 *V were on average* (83 ± 3) $\mu A/lm$ *and* (14 ± 1) mA/lm *respectively.*

while the anode luminous sensitivities varied by 29%. Note that these values were measured using a Tungsten filament lamp operated 2856 K, which produces light peaking around 1000 nm [26], far from the UV region. Given that the scintillation light from the CsI peaks at 315 nm, the Hamamatsu measurements of the cathode and anode luminous sensitivities may not be indicative of the PP performance in the ECL.

The final measurement provided by Hamamatsu was the cathode blue sensitivity index. The index is simply the cathode luminous sensitivity where the Tungsten lamp had a Corning Cs 5-58 blue filter at half-stock thickness filtering the light. This produces light with an emission spectrum that peaks at 420 nm [21]. Since the light has been filtered, it is not appropriate to use lumens as a unit of measurement, so Hamamatsu reports the value as a unitless quantity. The distribution of the cathode blue sensitivity index can be seen in figure 5.2.

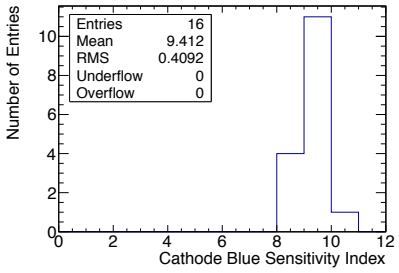

Figure 5.2: *Cathode blue sensitivity index as measured by Hamamatsu at* -750 *V. The index has an average of* 9.4 ± 0.1 *for the 16 PP.*

5.2.2 Gain vs Operating Voltage

Since the cathode luminous sensitivity is proportional to the quantum efficiency, and the anode luminous sensitivity proportional to the product of

the quantum efficiency and the internal gain of the PP, the quotient of the two is the internal gain of the PP. However, the Hamamatsu measurements were taken at an operating voltage of −750 V, whereas the measurements performed were taken at −1000 V. Additionally, since the endcap ECL will be in a magnetic field, it is expected that the gain of the PP will drop by roughly a factor of 3.5 [27]. To simulate this effect, and to correct the Hamamatsu measured gains to −1000 V, the peak locations of each of the calibration sources were tracked as a function of the operating voltage of the PP. Figure 5.3 shows the ADC location of the 1.063 MeV peak from the ^{207}Bi source as a function of PP operating voltage.

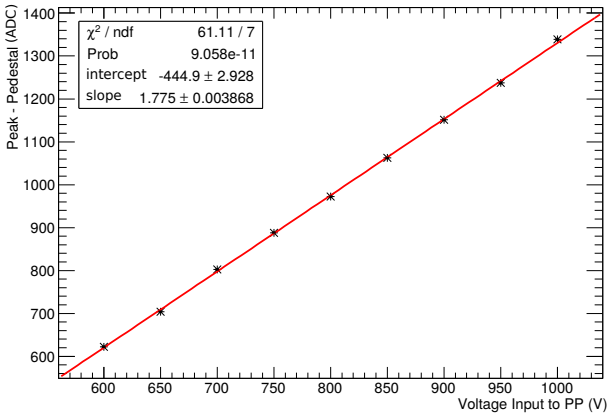

Figure 5.3: *To find the change in the gain, the peak location of the* 1.063 *MeV* ^{207}*Bi decay was tracked as a function of the PP operating voltage.*

Pictured in figure 5.4 is the distribution of the internal gains of the PPs at −1000 V, the nominal value. The average gain at −1000 V was 255 ± 11. The gain at any given voltage can be found by:

$$\text{Gain}(V) = \frac{\text{Peak}(V)}{\text{Peak}(-750)} \cdot \text{Gain}(-750), \tag{5.1}$$

where the gain at −750 V is given by the ratio of the luminous sensitivities by Hamamatsu. Figure 5.5 shows the average gain of all 16 PP as a function of the operating voltage, where the relationship between the operating voltage and the PP gain was seen to be linear. This was the case with all of the individual PP as well. Since the gain of the PP depends on the secondary emission ratio (δ) for each of the three dynodes, it was expected that δ would increase linearly with the voltage, and therefore the gain of the PP

would have increased non-linearly. It is perhaps due to the unequal voltage distribution to each of the dynodes that this was not the case.

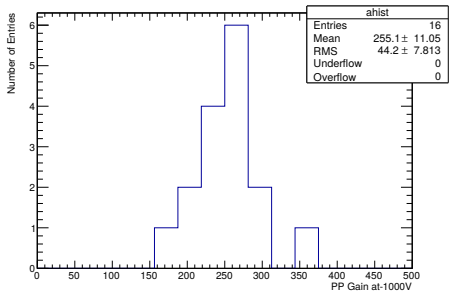

Figure 5.4: *The gain of the PP from the values measured by Hamamatsu, as predicted for an operating voltage of* -1000 *V.*

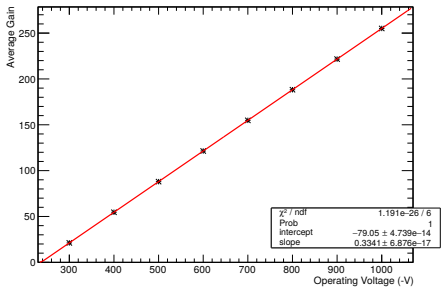

Figure 5.5: *The average gain of all PP as a function of the operating voltage. For each of the individual gains, see figure D.3.*

5.2.3 Comparisons

It is first important to note that the cathode and anode luminous sensitivities are intrinsically linked: the output of the anode for a given amount of light must depend on the effectiveness with which the cathode produces electrons. Figure 5.6 shows that the expected correlation between these two quantities is indeed present.

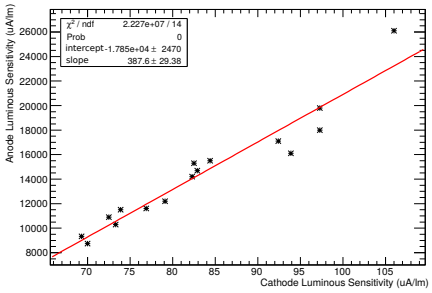

Figure 5.6: *The anode and cathode luminous sensitivities are correlated.*

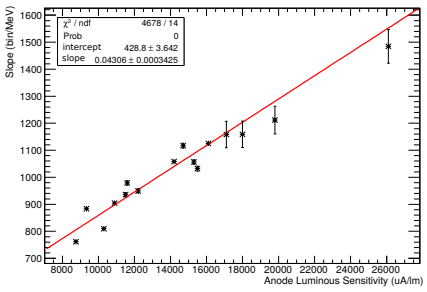

Figure 5.7: *The slopes from the peak vs energy plots as a function of the anode luminous sensitivity.*

The slope from the peak vs energy plots, as seen in figure 4.6, is a very similar measurement to the anode luminous sensitivity. Consider the units

of the slope: bin/MeV specifies the PP response as a function of the incident light, whereas the anode luminous sensitivity is a measure of the same with μA/lm. Additionally, both should depend on the sensitivity of the cathode and the anode. Figures 5.7, and 5.8 show the expected correlations are present. Additionally, with the blue filter present, the expected relationship still holds (fig. 5.9).

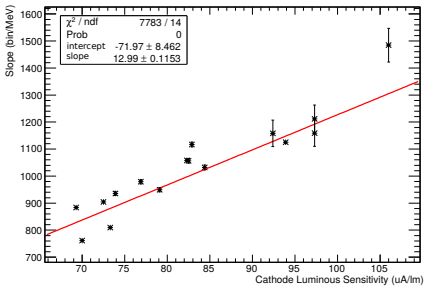

Figure 5.8: *The slopes from the peak vs energy plots as a function of the cathode luminous sensitivity.*

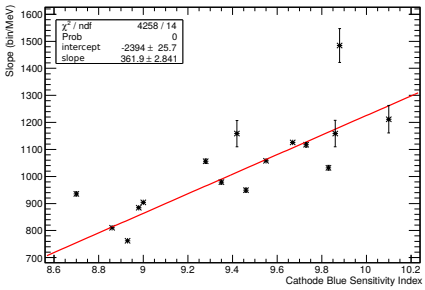

Figure 5.9: *The slopes from the peak vs energy plots as a function of the cathode blue index.*

Since both the slopes and the anode luminous sensitivity are measured at the anode, they should be dependent on the gain of the PP. Figures 5.10 and 5.11 show that this is indeed the case.

The cathode luminous sensitivity is proportional to the quantum efficiency. The anode luminous sensitivity is essentially the same as the cathode luminous sensitivity, but with the added factor of the gain. Therefore their quotient, the gain, should be independent of the quantum efficiency. This was not the case, as seen in figure 5.12. Furthermore, the component leftover from dividing the slopes by the gain should be correlated with the cathode luminous sensitivity. As seen in figure 5.13, this was also not the case.

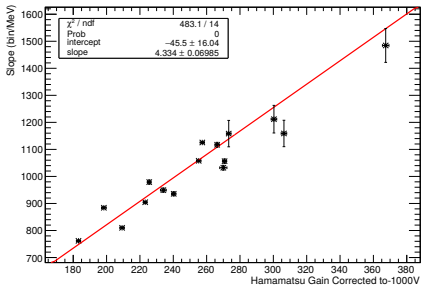

Figure 5.10: *The slopes from the peak vs energy plots are correlated with the Hamamatsu measured gains, corrected to the operating voltage of* -1000 *V. This was the voltage at which the peak locations were measured.*

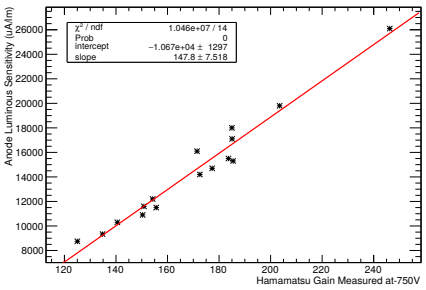

Figure 5.11: *The anode luminous sensitivity as a function of the gain measured by Hamamatsu.*

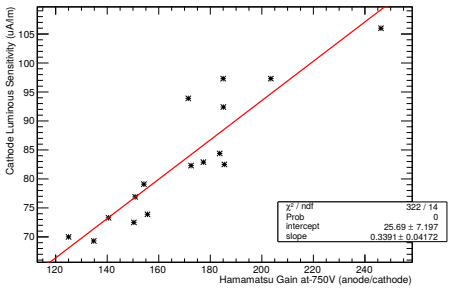

Figure 5.12: *The cathode luminous sensitivity as a function of the gain was seen to be correlated.*

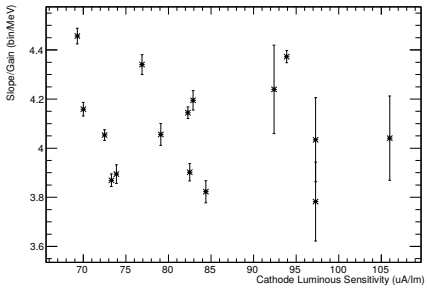

Figure 5.13: *The quotient of the slopes from the peak vs energy plots and the Hamamatsu measured gain corrected to* -1000 *V, as function of the cathode luminous sensitivity.*

It was observed that the slope/gain was not correlated with any other of the measured parameters, indicating that the variance in experimental setup may have increased the uncertainty of the measurement beyond expected levels. It should be emphasized that the slope/gain should be correlated with the cathode luminous sensitivity, as the slope is very similar to the anode luminous sensitivity and the anode sensitivity divided by the gain is

algebraically identical to the cathode sensitivity.

The quotient of the width and the peak location (the resolution), is a function of the energy deposited in the crystal, as seen in figure 5.14. Therefore, high energy events should expect a low resolution, less than 8% for signals above 2 MeV. The resolution was also found to be independent of the PP operating voltage.

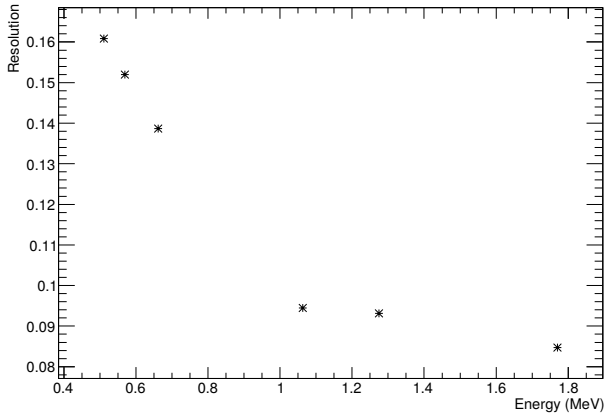

Figure 5.14: *Average resolution as a function of the energy. As expected, the resolution decreases with increasing energy deposit in the CsI.*

5.3 Conclusion

The Hamamatsu measured quantities were compared with the slope from the peak response vs energy plots. While correlations were observed between the slope and the anode luminous sensitivity, the cathode luminous sensitivity, and the cathode blue index, the experimental precision was not great enough to determine if a correlation was present with the PP gain factored out of the slope. There was also a correlation between the cathode luminous sensitivity and the gain.

Table 5.1 provides a summary of the average quantities measured for the 16 PP.

Furthermore, the gain was found to be linear with the operating voltage. This was an unexpected result, as a non-linear relationship was expected from the increased secondary emission ratios from the dynodes. It was also seen that the resolution improves with increased energy deposit in the CsI crystal.

Table 5.1: *Average Hamamatsu quantities which were measured at* -750 *V and the PP internal gain at* -1000 *V operating voltage for a population of 16 PP.*

Quantity	Average	Variation Among PP
Anode Luminous Sensitivity	(14 ± 1) mA/lm	29%
Cathode Luminous Sensitivity	(83 ± 3) μA/lm	13%
Cathode Blue Index	(9.4 ± 0.1)	4%
Dark Current	(0.011 ± 0.007) nA	64%
Gain at -1000 V	(255 ± 11)	17%

Chapter 6

Excess Noise Factor

6.1 Introduction

The excess noise factor is defined as the quotient of the squares of the resolutions at the cathode and the anode, as given in the following equation:

$$\left(\frac{\sigma_c}{N_c}\right)^2 F = \left(\frac{\sigma_a}{N_a}\right)^2, \tag{6.1}$$

where F is the excess noise factor, $N_{c,a}$ is the number of electrons at the photocathode and anode respectively, and $\sigma_{c,a}$ are the corresponding widths of the distributions [21]. The excess noise factor arises because of the multiplication process in the photopentode (PP), as described in chapter 2.

Taking advantage of the Poisson distributed nature of the photoelectrons, this can be re-written in the following linear form:

$$\sigma_m^2 = F \cdot N_c + \sigma_o^2, \tag{6.2}$$

where σ_m is the width of the signal in units of number of photoelectrons and σ_o is the electronic noise. For details on the algebraic manipulation see appendix C.2. Recall that an electron at the cathode is named a photoelectron, and therefore the goal of this measurement was to extract the excess noise factor by observing the width of the output distribution as a function of the number of photoelectrons.

6.2 Experimental Setup

Originally, the idea was to use a standard PMT (appendix B.2.3) to count the number of incident photons, and to use the width of the signal produced by the PP to determine the excess noise. This idea was discarded because it was not possible to isolate the quantum efficiencies of the two phototubes, both of which are unknown quantities. It was only possible to find their ratio (appendix C.4), which could only be solved for in such a way that using the standard PMT was redundant. A full justification of why the

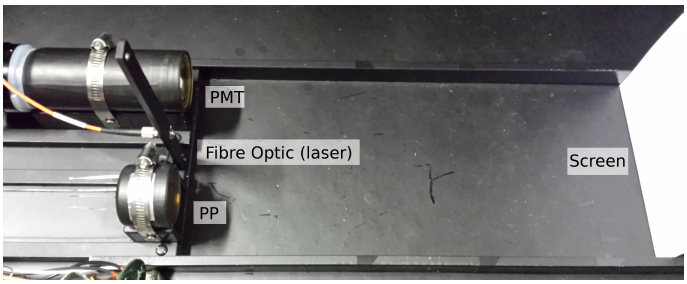

Figure 6.1: *Excess noise setup top view. This setup was encased in the dark box with the laser light being transmitted via fibre optic.*

standard PMT was not useful can be found in appendix C.3. Despite this, even the latest iteration of the setup incorporated this idea into its design. As seen in figure 6.1, the setup consisted of four parts: the phototubes, the screen, the fibre optic, and the support structure. The PMT and the PP were run at the operating voltages of -2200 V and -1000 V respectively.

The laser was the source of UV light in this measurement. It produced variable intensity pulsed UV light of 405 nm at an adjustable rate (appendix B.2.4). In this case, the pulse rate used was 350 Hz. The laser itself was kept outside of the dark box, and the light was transmitted into the box by fibre optic and optical feedthrough. The use of the laser was motivated by the ease at which one could adjust the light intensities, as well as the range of intensities available.

To ensure that the light was uniform across the face of both phototubes, a diffuse screen was used to reflect the laser light (appendix B.2.5). The screen was held perpendicular to the phototubes, and the phototube to screen distance could be changed to adjust the light intensity, in addition to varying the laser voltage. This was needed because the laser required that the voltage be set beyond a threshold, effectively setting a minimum nonzero intensity for the light produced. To further lower the light intensity, the screen was moved further away from the phototubes.

The support structure housed all the components. The purpose of this device was to ensure that the screen, PP, PMT, and laser were all secured in place with respect to each other. The screen was allowed to slide within a track, allowing the distance between the screen and the phototubes to change while keeping the screen perpendicular to the plane of the faces of the phototubes. The support structure also had a port in which the fibre optic was installed, and could be rotated to adjust the position of the light on the screen. The two phototubes had custom built supports to secure the

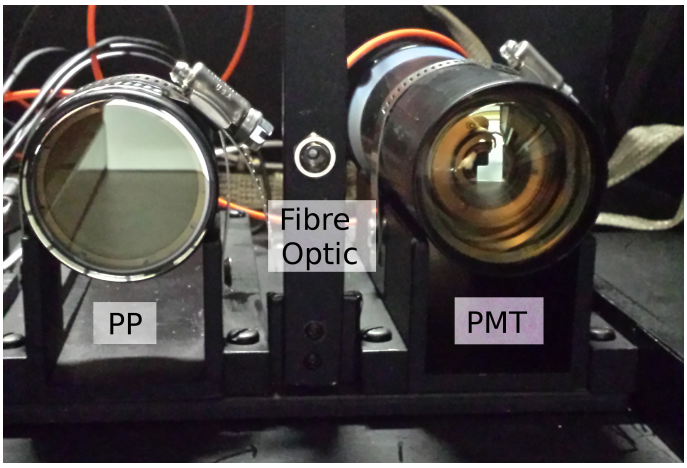

Figure 6.2: *Excess noise setup front view. The PP and the standard PMT were held in parallel so that they received the same amount of light. The angle at which the laser was held relative to the screen was adjustable.*

phototube in place, and each could be exchanged in a reproducible manner. Upon exchange, the angle at which the phototube was held did not change, nor would the distance between the phototube and the screen. Figure 6.2 shows the portion of the support structure that housed the phototubes and the fibre optic.

The DAQ for this measurement again made use of the peak sensing LeCroy L2259B ADC, and the MIDAS software. The ADC gate was provided by a NIM signal that was coincident with the TTL signal sent to trigger the laser. Since the standard PMT did not need a preamp or shaper, the ADC used to measure the output was an integrating ADC, the LeCroy L2249. Both were triggered simultaneously. The output of the standard PMT was attenuated by a factor of 0.3, to ensure that the output signal was within the range of the L2249 ADC. With similar reasoning, the output of the Ortec 474 shaper was amplified by a factor of 10. For more details please refer to appendix A.3 for the circuit diagrams.

6.3 Results

6.3.1 PMT Single Photon Measurement

During the time it still seemed likely that the standard PMT would be used, it was instructive to determine the gain of the standard PMT. A small

light leak was introduced in the dark box by leaving the optical feedthrough disconnected from the fibre optics. Using a random trigger, single photons could be found by hand on a Tektronix Oscilloscope. A series of single photon waveforms were saved and were then integrated in ROOT. With the 50 Ω input resistance of the scope and cables, the equivalent charge for each waveform was calculated and histogrammed, as seen in figure 6.3. Dividing the histogram mean by the charge of an electron, indicates that the gain of the R5113-02 PMT was $(3.99 \pm 0.15) \times 10^6$ with the attenuation.

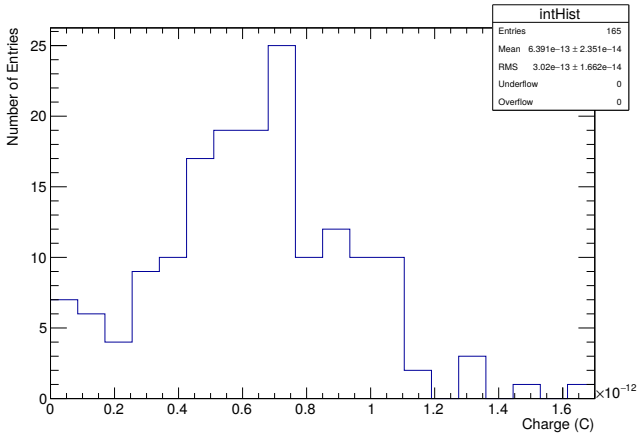

Figure 6.3: *Single photon measurements made with a 0.3 attenuation on the output. The PMT gain, including attenuation, was found to be* $(3.99 \pm 0.15) \times 10^6$.

6.3.2 Time to Stabilization

It was observed that the signal from the PP varied significantly when the laser was first turned on, prompting an investigation as to the length of time until the PP signal stabilized. For this measurement, the conditions arising from switching the phototubes or adjusting the screen position were mimicked: both the laser and the phototube operating voltage sources were turned off, and the dark box was left open for about 15 minutes. The dark box was then closed, and both power sources were turned back on. The amplitudes of the PP signal were then immediately recorded in 120 second segments over the next hour. An example of the resulting spectrum from one such segment can be seen in figure 6.4, with Novosibirsk fit. The Novosibirsk function was chosen because the distribution was found to be asymmetric.

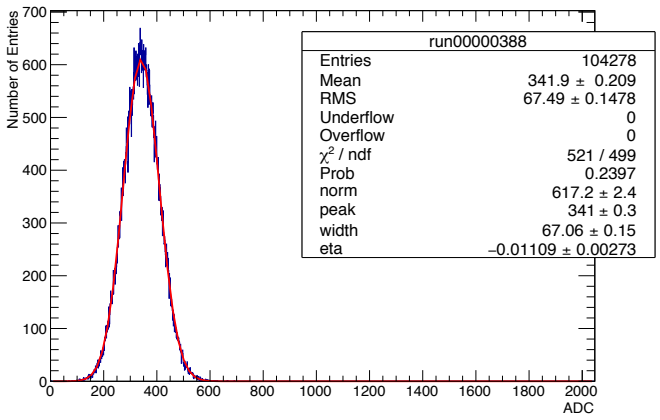

Figure 6.4: *Peak height spectrum from pulsed laser as measured by the PP, with Novosibirsk fit. The peak location and width of this fit are used to determine the excess noise factor.*

See appendix D.5 for a comparison with a Gaussian fit.

It was found that after about 15 minutes, the variation in the amplitude of the PP signal was less than about 0.5% and that this was no longer a significant source of uncertainty in the final measurement. The stability of the system can be seen in figure 6.5, a histogram of the same value found in figure 6.6. After fitting the normalized histogram with a Gaussian, the stability was measured to be $(0.38 \pm 0.06)\%$ over the course of an hour.

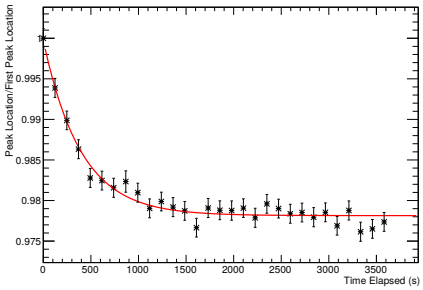

Figure 6.5: *Time to stabilization for the PP and laser setup. The curve was fitted with the sum of an exponential and a constant to help determine the ideal point at which the PP could be considered stabilized (15 minutes).*

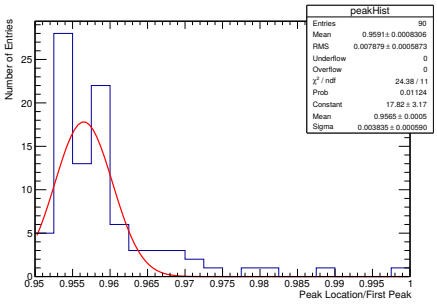

Figure 6.6: *The peaks from the Novosibirsk fits over the course of an hour. Here, the histogram has been fitted with a Gaussian, to show that the variability in pulse height is* $(0.38 \pm 0.06)\,\%$.

6.3.3 Uncertainty of Measurement

To determine the reproducibility of the setup, the phototubes were exchanged several times, each time taking a measurement of the incident light. Each run had the same light intensity setting, and allowed the setup to stabilize for the established period before a measurement. The uncertainty, as shown in figure 6.7, was 4% in one position and 3% in the other position. Despite the lack of phototube exchange in the final measurement, this should be taken as an estimate of the uncertainty in incident light as the PPs were cycled through.

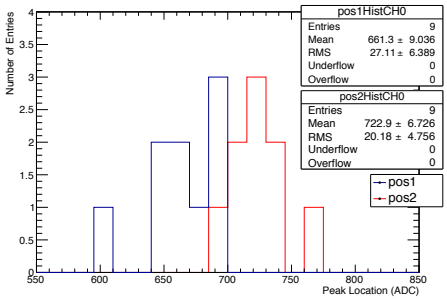

Figure 6.7: *The reproducibility of the PP measurement after exchanging the phototubes.*

6.3.4 Calibration Pulse Measurement

To convert the MIDAS signal to the number of photoelectrons, it was first necessary to convert the bins read from the ADC into the amount of charge at the anode of the PP. This was done with the aid of the calibration test

pulse input of the preamp. The test pulse allowed for the injection of a given amount of charge into the preamp to simulate a real photon event. The mechanism for the injection was a (1 ± 0.25) pF capacitor [23]. A pulse generator was used to send square waves of width 127 μs into the capacitor, and the capacitor converted the input voltage into a pulse of corresponding charge. A screenshot of the output calibration pulse after the shaper and x10 amplification can be seen in figure D.10.

The input charge to the preamp was then varied and the corresponding ADC signal observed, as seen in figure 6.8. The pedestal used here was the same as was found with the energy linearity measurements in chapter 4. It was found that the conversion rate from the ADC bin to charge at the PP anode was $(8.54 \pm 0.03 \pm 1.3) \times 10^{-18}$ coulombs / bin.

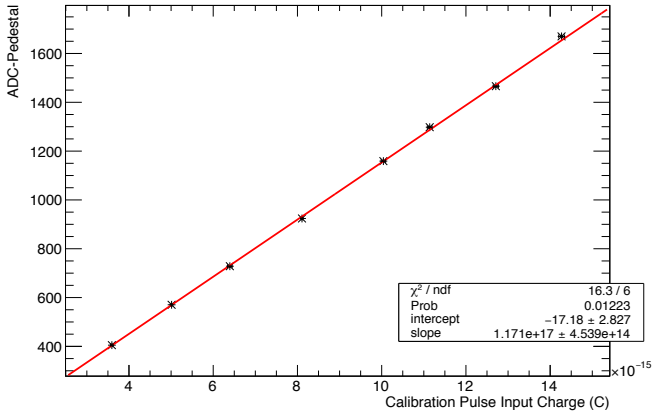

Figure 6.8: *Calibration pulse results, with a linear fit. This allows for the conversion from ADC bin to charge at the anode of the PP:* $(8.54 \pm 0.03 \pm 1.3) \times 10^{-18}$ *coulombs / bin.*

6.3.5 Excess Noise Factor

As was outlined in section 6.1, the goal of this chapter is to measure the width of the signal and to plot this as a function of the signal peak, in units of number of photoelectrons. To this end, recall that

$$\sigma_m^2 = F \cdot N_c + \sigma_o^2, \tag{6.2}$$

where σ_m is the width of the signal measured, N_c is the signal size at the cathode, and σ_o is the electronic noise, and all are in units of number of

photoelectrons. The strategy employed was to change the incident light intensity by varying the screen to PP distance and to record the resulting signal height distribution. This spectrum was fitted with a Novosibirsk function, and the peak height and width for each light intensity were recorded in ADC counts. The pedestal from chapter 4 was subtracted. The calibration pulse measurement described in section 6.3.4 was used to convert the ADC value to charge at the anode. The anode charge was then divided by the gain and the charge of an electron to get the number of photoelectrons. The result of the above operations on both the width and the peak locations can be seen in figure 6.9.

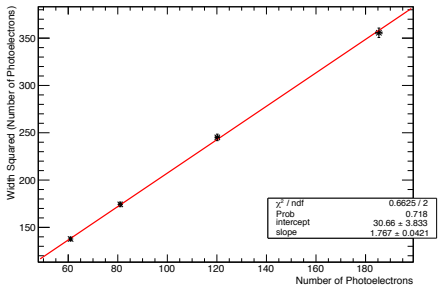

Figure 6.9: *Excess noise factor calculation for a single PP. The excess noise factor for this PP was* 1.77 ± 0.04*, and the electronic noise was* 5.5 ± 0.3 *photoelectrons.*

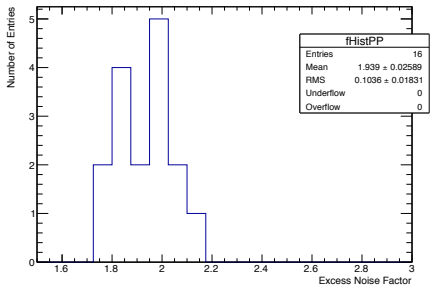

Figure 6.10: *Histogram of all the excess noise factors of the acquired PP. The mean excess noise factor was* 1.9 ± 0.1*.*

The fit in figure 6.9 is simply equation 6.2, and therefore the slope is the excess noise factor and the intercept is the square of the electronic noise. The excess noise factors for all of the 16 PP can be found in figure 6.10, and the electronic noise in figure 6.11. The average excess noise factor from all the PP was $(1.9 \pm 0.1 \pm 0.4)$, with the systematic error arising from the uncertainty in the preamp test pulse. The average electronic noise was found to be 1730 ± 33 electrons at the anode, or

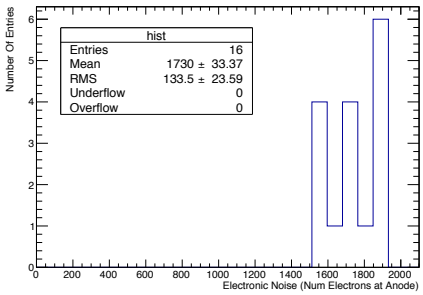

Figure 6.11: *Histogram of all the electronic noise values (should be independent of PP), in units of number of electrons at the anode. There is 7.7% variability in the measurement.*

equivalently (32 ± 1) keV from the Saint-Gobain CsI crystal.

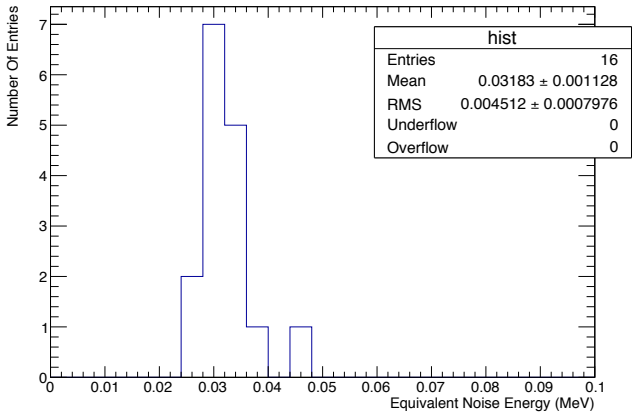

Figure 6.12: *Histogram of all the electronic noise values, in units of equivalent energy from the Saint-Gobain CsI crystal. Note that this value is much smaller than the noise found in chapter 3, showing the difference in crystal quality.*

6.3.6 Excess Noise at Reduced Operating Voltage

Since the ECL is in a magnetic field, it is expected that the gain will drop by a factor of about 3.5 [27]. To simulate this, the operating voltage of the PP was reduced and the excess noise factor measurement discussed in the previous section was repeated for each voltage setting (fig. 6.13). The excess noise factor was found to increase for operating voltages below -400 V, or a gain of about 55. Above this, there was no significant relationship between the operating voltage and the excess noise factor.

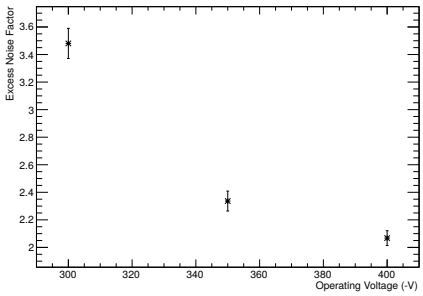

Figure 6.13: *Excess noise factor as a function of operating voltage, at less than 1/3 of the maximum gain. See figure 5.5 for details on the gain.*

6.4 Conclusion

The average excess noise factor for the R11283 Hamamatsu photopentode was found to be $(1.9 \pm 0.1 \pm 0.4)$ at a gain of 255 (-1000 V), and increasing to 3.5 ± 0.1 at a gain of 25 (-300 V). The large systematic error arose from the 25% uncertainty in the preamp test input capacitor [23]. The trend seen in the PP is the inverse of that seen in avalanche photodiodes (APD), where the excess noise factor increases with gain [28]. The PP starts to become competitive with the cited APDs at a gain larger than ≈ 50 (-350 V). Given that the gain of the particular PP tested would drop to about 105 in the magnetic field, it is expected that the performance will be better as well. Note also that the PP holds up when in direct competition with the Hamamatsu S8664-1010(S8664-55) APDs for use in the Belle II ECL, where the excess noise factor was found to be $3.4 \pm 0.4(5.1 \pm 0.5)$ [29].

The electronic noise of the preamp was also found in units of number of electrons at the anode, 1730 ± 33. This is comparable to the value measured by the Université de Montréal, 1500 e^- [23]. The equivalent noise energy was also be found from this measurement, and was reported as (32 ± 1) keV for the polished pure CsI crystal provided by Saint-Gobain; less than half of the value found for the large BINP CsI crystal in chapter 3. This discrepancy is likely due to the difference in crystal quality, size, and polish. It should be noted that measuring the RMS of the spectrum of waveform heights is not sufficient to make a measurement of the electronic noise, since the excess noise factor is not taken into account.

Chapter 7

Aging and Lifetime

7.1 Introduction

The primary result needed from the photopentode (PP), as outlined in the Belle Technical Report [6], was the lifetime of the PP. To do this, UV light comparable to the dominant wavelength of the pure CsI emission spectrum was flashed on a array of 16 PP (fig. 7.1) for about 48 days. A ^{207}Bi source was used to track the performance of the PP. Approximately 70 years worth of Belle II operation was simulated in this manner, and the change in PP performance and stability was measured.

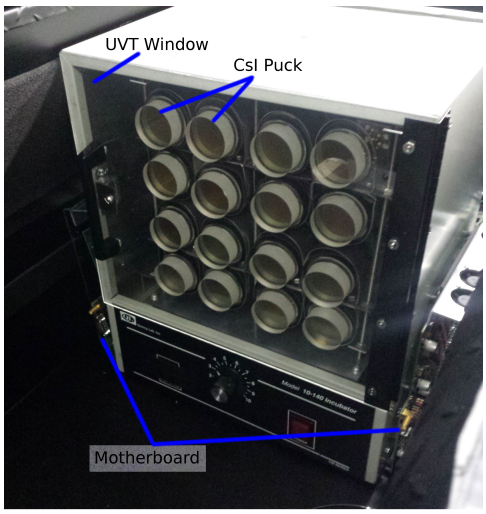

Figure 7.1: *PP array encased in incubator with glued CsI pucks.*

The predicted maximum radiation dosage rate in the ECL is about 1.3Gy/yr [30], and the large Belle II BINP crystal has a light yield of 185 photoelectrons per MeV [31]. For 7 years of operation there should be about (2.84×10^{14}) MeV deposited in the crystal. With the PP internal gain assumed to be $\frac{250}{3}$ in the $\vec{B}$ field, this corresponds to 0.701 C at the anode. As a safety factor, a total charge an order of magnitude larger was induced in the anodes.

7.2 Experimental Setup

It was thought that the amount of current passed by the anode of the PP was the primary cause of the PP aging. An array of 16 PP was built to study the effects of aging. The array was read out using the V4 preamp, in conjunction with the Université de Montréal shapers (appendix B.1.2). Each PP had its own two inch diameter pure CsI puck provided by Amcrys glued to its face using a silicone rubber glue (appendix B.2.2). The PP array was encased in an incubator set to keep the temperature at roughly 35 °C (appendix B.3.5). The incubator was outfitted with a UVT acrylic door, and N_2 was pumped into the top of the incubator to help keep the humidity low. The humidity and temperature sensor was placed inside the incubator, along one of the walls.

To accelerate the aging process, an LED flasher provided by the University of McGill (appendix B.2.6) was used to induce a large current through the PP dynodes and anode. Figure 7.2 shows the LED flasher and incubator setup. The flasher was set to a distance of about 40 cm from the PP array and was run with a DC power source set to induce about 2 μA of current through the anode. The current at the anode was measured directly on one of the PP by means of a modified preamp (appendix B.1.3). The current was read out by the Keithley 6485 Picoammeter, and the result recorded with MIDAS. To track the stability of the PP, a ^{207}Bi source was used. This was taped to the mechanical support structure holding the LED array. As

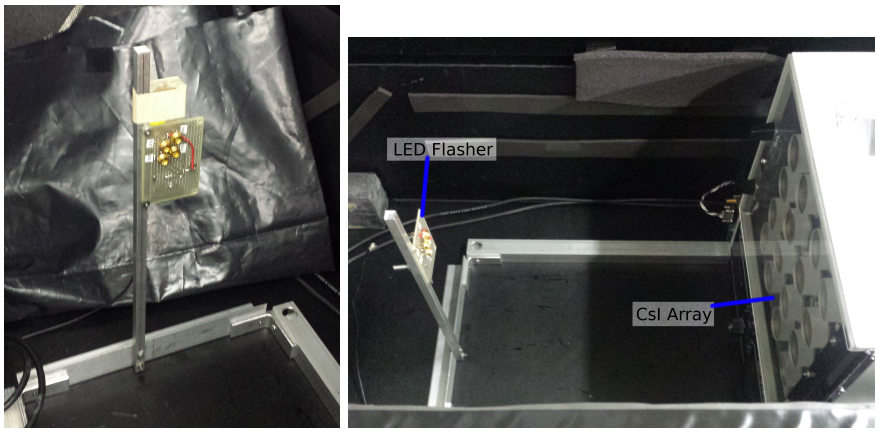

(a) *LED Flasher with ^{207}Bi source attached.* (b) *LED Flasher and PP array in incubator.*

Figure 7.2: *Setup for aging the PP in the dark box.*

mentioned, the gain of the PP array was kept at a third of its maximum value by setting the operating voltage to 491 V, with the exception of the two lowest gain PP where the operating voltage was set to 618 V. This was done to ensure that the peak locations remained within the range of the ADC while the PP was aged. The average gain of the 16 PP at 491 V was 85 ± 3. Refer to appendix A.4 for the associated circuit diagram.

7.3 Results

7.3.1 Current Baseline and Estimation

To estimate the current in each of the PP while the aging was ongoing, the current of each PP was first measured under identical conditions. Each PP was done in sequence, with three repetitions of the sequence. Since only one of the PP had the current measured throughout the entire aging process, the currents from the baseline measurement were compared to provide an estimate of the current passing through the anode of each PP. Equation 7.1 describes the estimated current in the j^{th} PP (I_j), given the currents from the baseline measurement ($I_j^{(B)}$):

$$I_j = \frac{I_j^{(B)}}{I_r^{(B)}} I_r, \tag{7.1}$$

where I_r is the current measured from the reference PP with the modified preamp. Given that not all of the PP were run at the same operating voltage, the relationship between the current and the operating voltage was established and can be found figure B.5.

7.3.2 Aging and Lifetime

Figure 7.3 shows the cumulative charge passing through the anode of the monitoring PP as a function of time. This curve is the result of integrating the current with respect to time. The raw current measurement can be seen in figure D.11 in the appendix. Approximately 7 C of charge was passed through the anode over 48 days.

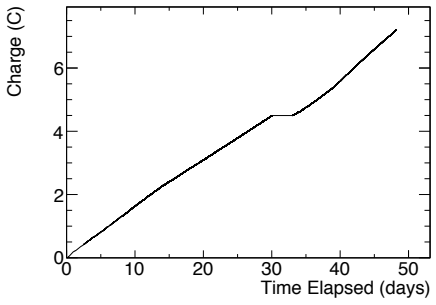

Figure 7.3: *The total charge passed through the anode of the current monitoring PP.*

Figure 7.4 shows the spectra of the LED aging light pulses. Since the LED array was run with a DC current, the DAQ recorded a range of small pulses at a rate of about 1 MHz. This is ideal for the aging as a large number of low energy events is the expected form of the background in the Belle II ECL. The ^{207}Bi spectrum in figure 7.5 was fitted with the sum of two Novosibirsk functions and an exponential. The exponential roughly models the backscattering and background from the other peaks, while the Novosibirsk captures the location of the peaks. It is the peaks of the Novosibirsks that was used to track the performance of the PP.

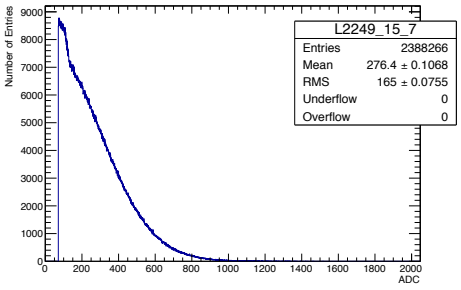

Figure 7.4: *Distribution of the pulse heights from the LED used to age to the PP.*

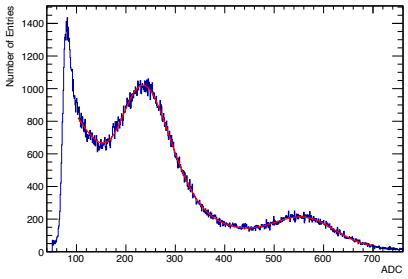

Figure 7.5: *Spectrum of the pulse heights due to the ^{207}Bi source, with fit. The peak locations were used to track the PP performance.*

There was a pedestal in the measurements, where the projected output of the ADC for zero energy was non-zero, which was due to a DC offset in the shaper output. To find the offset for each of the PP, a three hour measurement of the ^{207}Bi spectrum was taken and all three peaks were fitted with the sum of three Novosibirsk functions and an exponential. The increased time of the run was needed to accurately see the highest energy decay (appendix D.7). The peak locations were then plotted as a function of the energy deposited in the crystal (fig. 7.6),

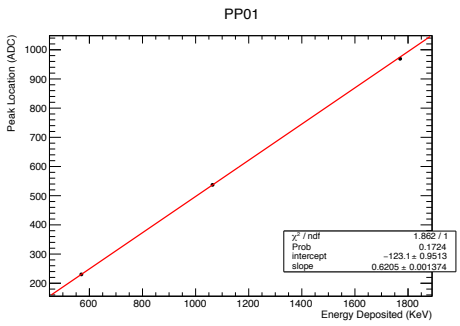

Figure 7.6: *Typical ^{207}Bi peak locations as a function of energy. The spectrum was measured over the course of a three hour period in order to get the statistics necessary to see the third peak.*

and the intercept of the linear fit was then subtracted from all the measured peak locations during the aging process.

Figure 7.7 displays the temperature and humidity reading from inside the incubator. It was noted that the temperature was held within about 2 $°C$ and the humidity within about 5% relative humidity, with allowances for the system to stabilize at the beginning. Because the system was not in thermal equilibrium, the first measured ^{207}Bi spectrum was discarded, as it was taken within this time.

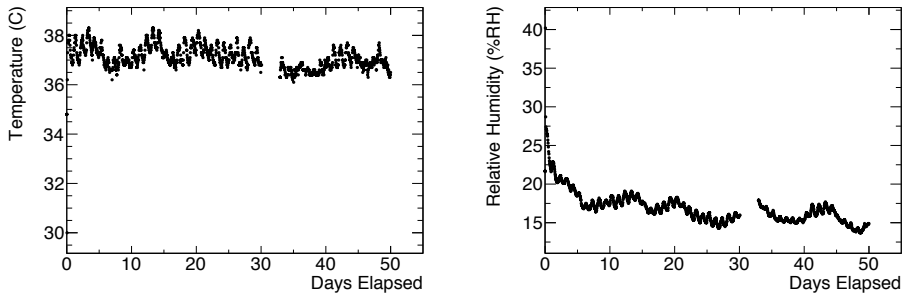

(a) *Temperature* (b) *Humidity*

Figure 7.7: *Temperature and humidity were recorded in the incubator. Note that this does not reflect the conditions outside of the incubator, where the LED flasher was placed.*

Figure 7.8 shows the temperature dependence of the ^{207}Bi peaks of the control PP, with linear fit. It was seen that the effects due to temperature were not large, with most corrections to the peak location at the level of 1-2%, after pedestal subtraction. It was found that the temperature dependence of the PP did not vary much from tube to tube, and so each peak of every PP was corrected by the corresponding peak from the control PP, after pedestal subtraction.

Using the ^{207}Bi source and the Amcrys CsI crystals, the 0.57 MeV peak varied by $(-1.3\pm0.6)\%/°C$ and the 1.064 MeV peak varied by $(-1.2\pm0.4)\%/°C$. In comparison, the ^{137}Cs source and St. Gobain CsI crystal from chapter 4.3 produced a temperature variation of $(-1.65 \pm 0.02)\%/°C$.

Figure 7.9 compares the product of the gain and the quantum efficiency between the control PP and an aged PP.

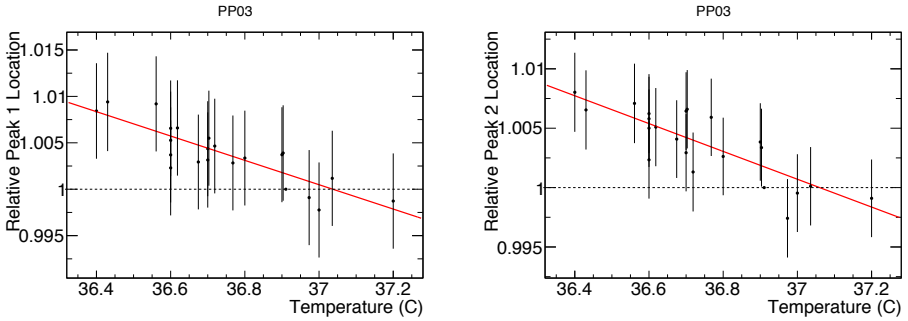

(a) *The 0.57 MeV peak varied by* $(-1.3 \pm 0.6)\%/^{\circ}C$.

(b) *The 1.064 MeV peak varied by* $(-1.2 \pm 0.4)\%/^{\circ}C$.

Figure 7.8: *Variation of the* ^{207}*Bi peaks of the control PP with temperature, after the aging was completed.*

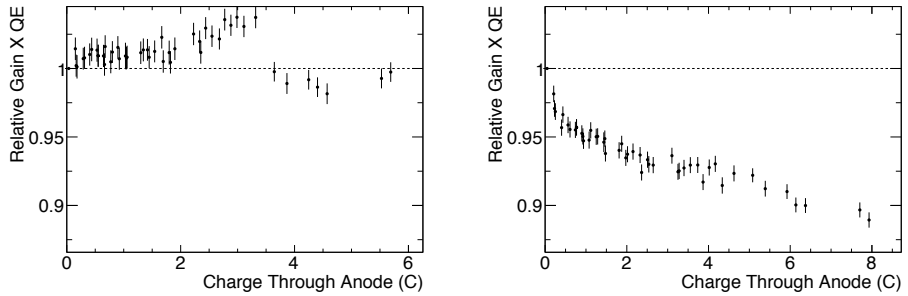

(a) *The control photopentode (PP03).*

(b) *An aged photopentode (PP16).*

Figure 7.9: *The slope of the peak location as a function of energy, relative to the first measurement. In the case of the control PP, the current is that which would have been flowing through the anode, if the PP was not capped.*

Recall that the gain $\times$ quantum efficiency comes from the slope of the peak location vs energy plots. In this case, the slope comes solely from the first two peaks, as there was not enough statistics in the one hour runs to distinguish the third peak. While this aged PP's performance decreased by about 10%, it was seen that the control PP's performance improved by about 5% before returning to its initial state. The reader may have observed a plateau in the cumulative charge at about day 31 (fig. 7.3). When the charge is converted to the charge in the control PP, this plateau corresponds to the drop in the control PP's performance at about 3.5 C. At this time, there was a severe storm which knocked out the power at TRIUMF, and the

experiment was left without power for about 2 days. It is unknown as to why this would have affected the control PP in this way. There may be some benefit to studying the change in the response when a delay in operation is introduced. In contrast, the storm did not seem to affect the aged PP overly much, suggesting that the change in performance due to aging is real. Figure 7.9b is not typical of an aged PP.

As seen in figures 7.10 & 7.11, there seemed to be four main trends in the PP aging:

1. Performance that aged quickly (a burn-in), and then stabilized to a constant level of performance (green borders in figures 7.10 & 7.11).

2. Performance that had the burn-in period, but never stabilized. Typically, this trend ended with what appears to be a linear dependence on the charge (blue).

3. Performance that decreased steadily throughout the aging process and did not show the burn-in period (black).

4. Performance that did not change, or increased, throughout the aging process (red).

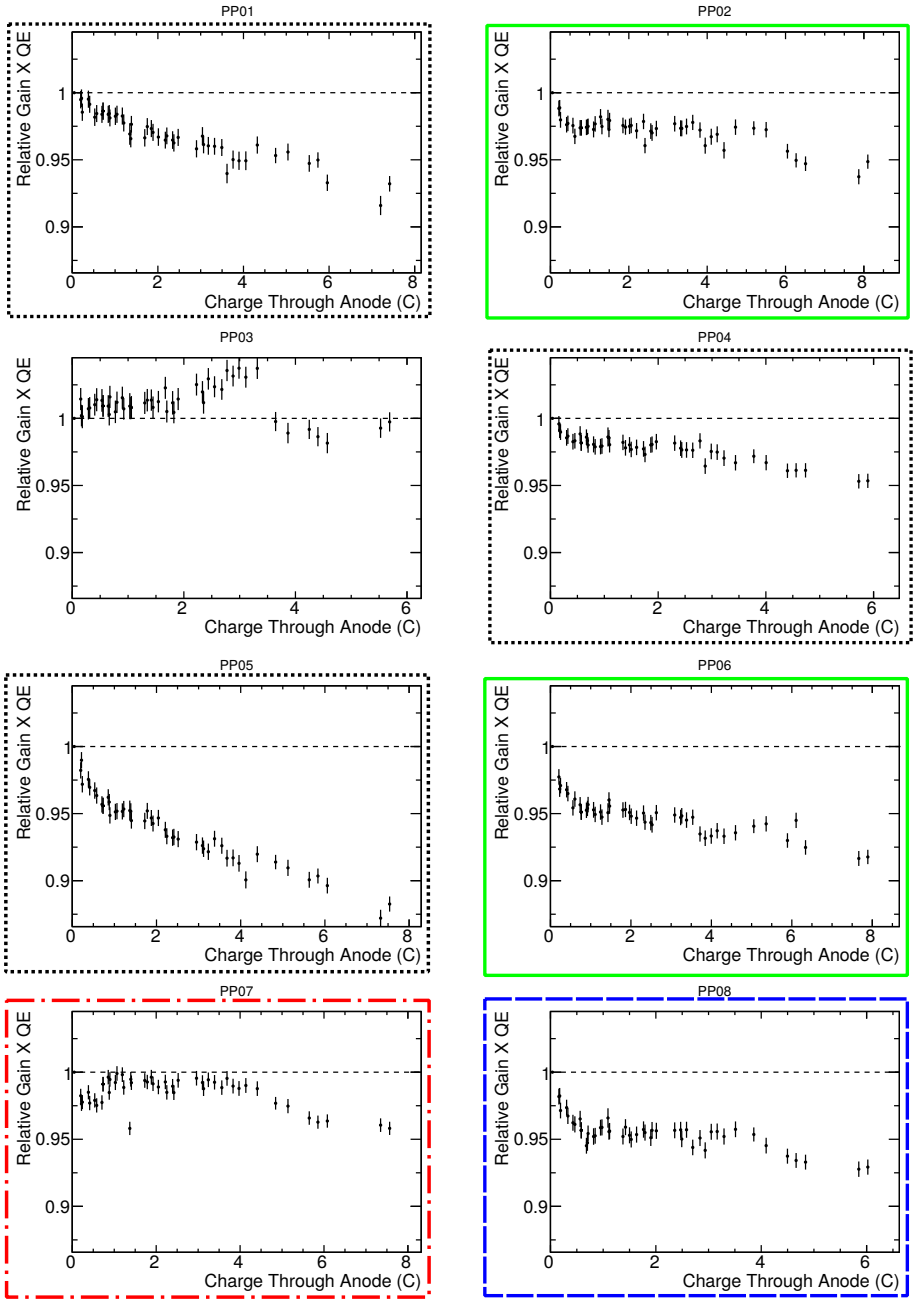

Figure 7.10: *The slopes of the peak vs energy deposited for only the first two peaks, relative to the first measurement, as a function of the charge passed through the anode. PP03 is the control PP. These results have been corrected for variations in temperature.*

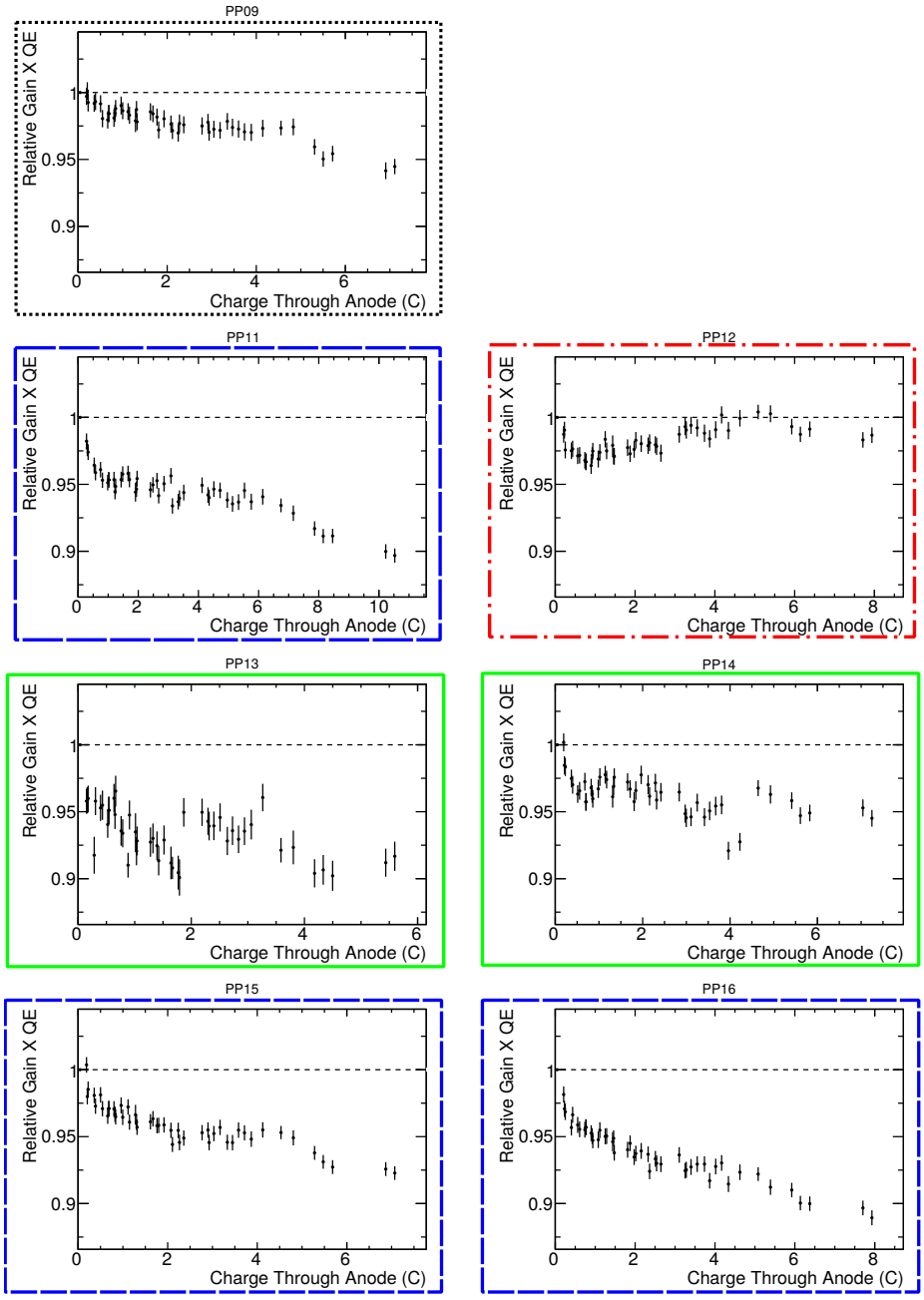

Figure 7.11: *The PP have been divided into four categories: aged for a period, then stopped (solid); aged, but didn't stop (− − −); aged at a constant rate throughout (· · ·); and no aging at all (− · −). PP10 is the reference PP, with the modified preamp to measure current.*

For additional details on the categorization of the PP, refer to appendix D.7. It should be noted that only PP07 had a significantly different history from the rest: this was the PP that was used to set up the excess noise factor measurements, and was used extensively with the pulsed UV laser for a few months. For the PP that experienced the burn-in, most of the aging occurred in the first coulomb of current having passed through the anode. It should also be noted that the pedestals which can be acquired from the first two peaks varied by about 5% prior to the pedestal subtraction, and was not correlated with the gain × quantum efficiency.

On average, the gain × quantum efficiency decreased to $(93 \pm 3)\%$ of the original performance. This is seen the following section, where the stability of the PPs was measured after the aging was finished. Figure 7.12 shows the average of the last 10 measurements after the aging was completed for all PP.

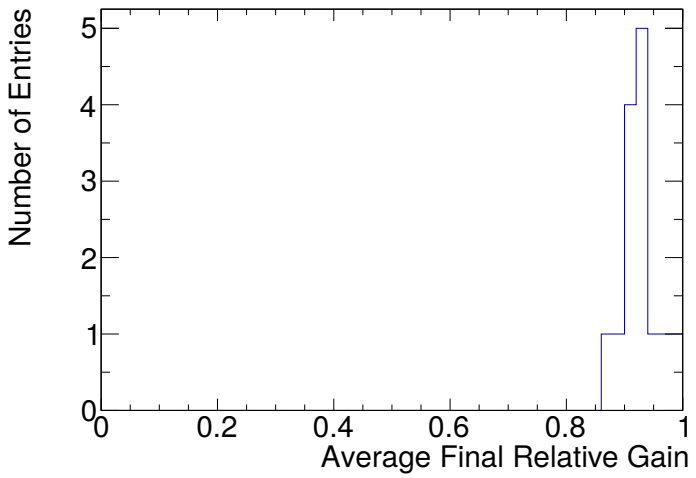

Figure 7.12: *Distribution of the relative gain × quantum efficiency of each PP averaged over the last 10 measurements. The full spectrum of measurements can be seen in figures 7.13 & 7.14. This distribution has an average of* $(93 \pm 3)\%$.

7.3.3 Post-Aging Stability

After the aging process, the ^{207}Bi spectra continued to be measured at regular intervals over the course of about 10 days, but the LED array remained off. The measurements with no light source can be seen appended the vertical dotted line in figures 7.13 & 7.14.

PP02 appears to have some instability present, as there was about a 10% change in the performance after the LEDs was turned off. It was also seen that perhaps some of the aging is not due to the LED as PPs 1, 4, 7, and 9 all appear to continue aging with no light source. The rest of the PP appear to have a more expected behaviour, with the performance stabilizing at the aged level and staying mostly constant. It is worth noting that with the post-aging measurements, the control PP effectively experienced zero change in performance.

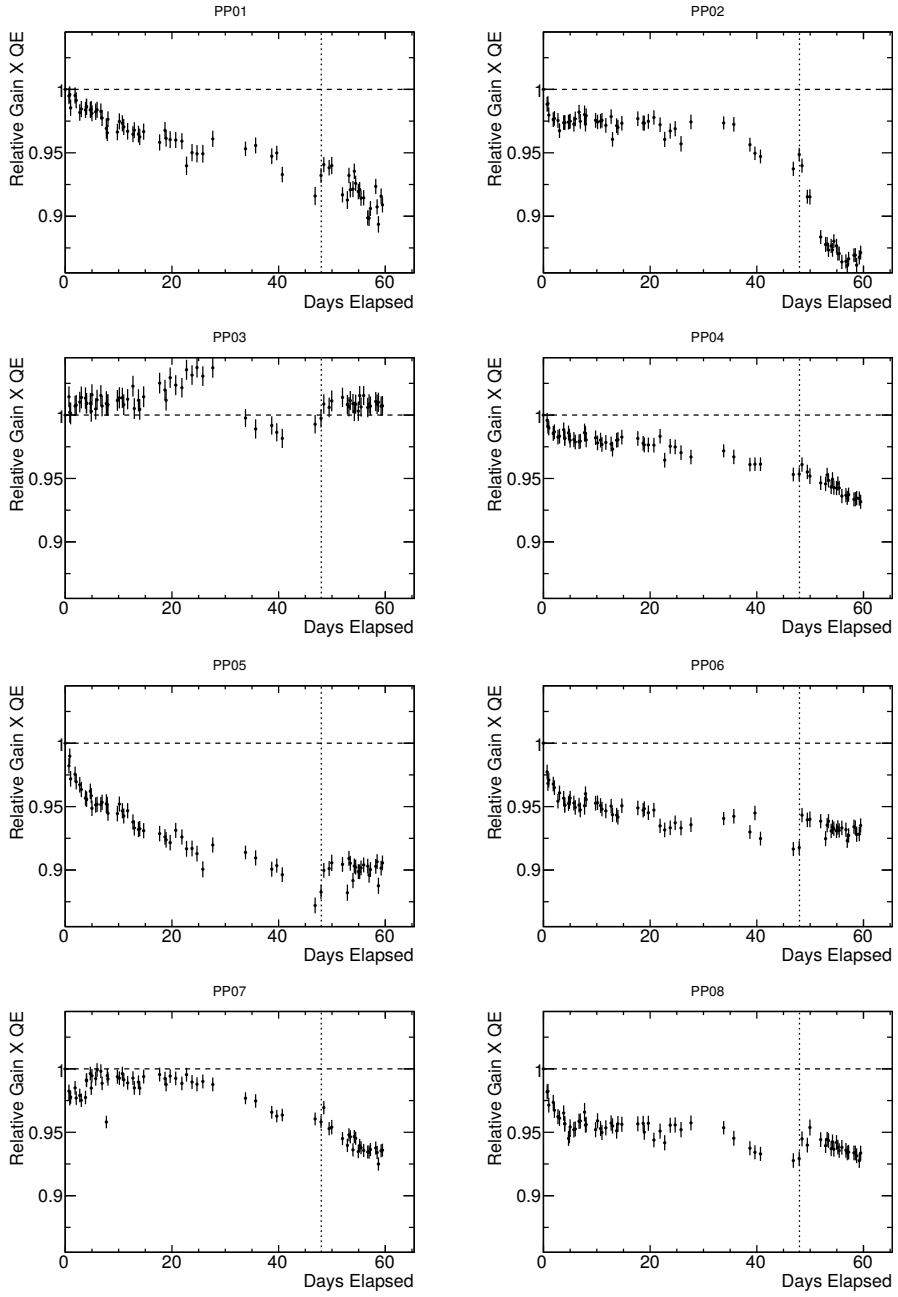

Figure 7.13: *Relative gain × quantum efficiency as a function of time elapsed in the laboratory. These results have been corrected for temperature variations.*

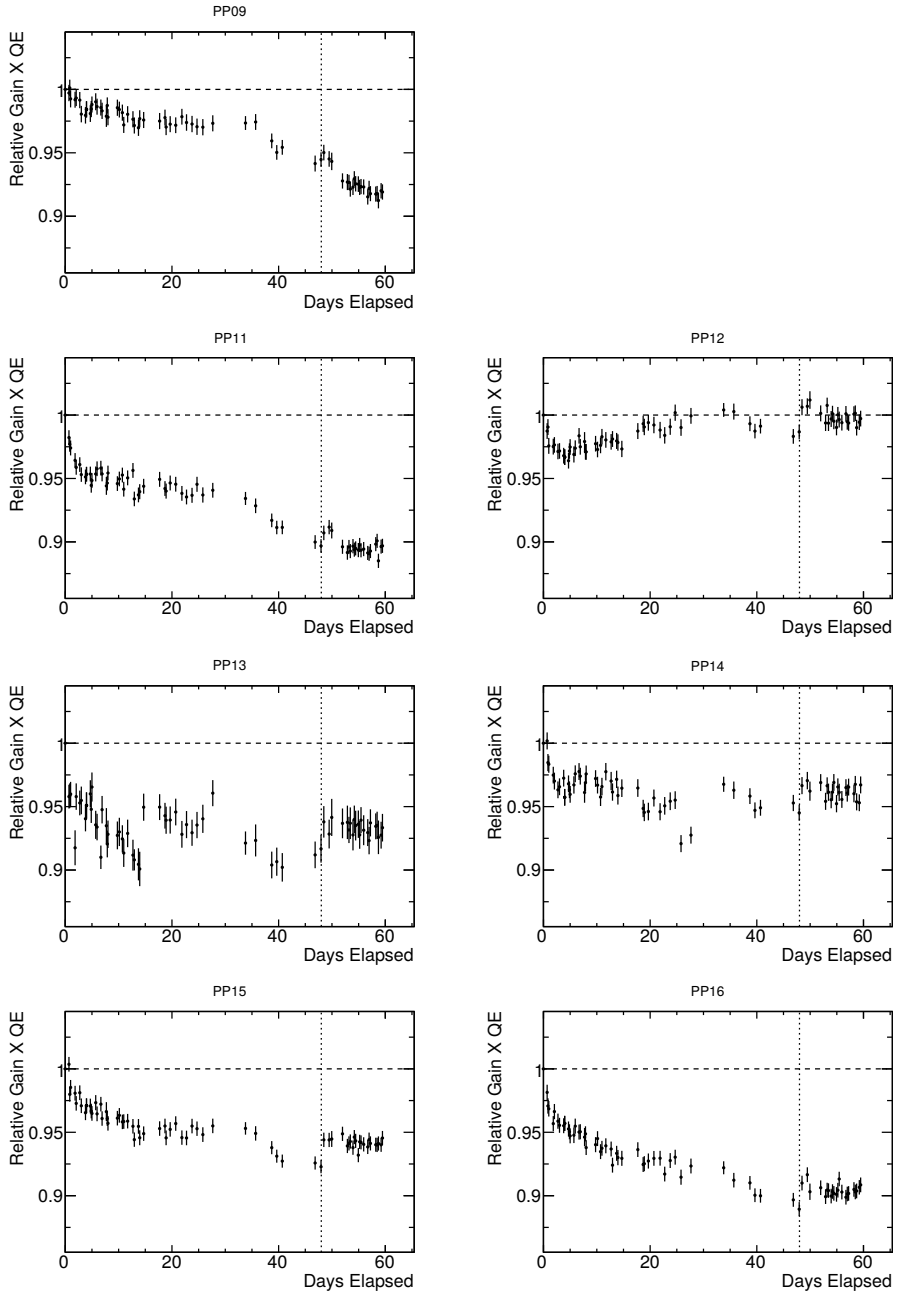

Figure 7.14: *The LEDs were switched off after 48 days, marked by the vertical dotted line. PP10 is the reference PP, with the modified preamp to measure current.*

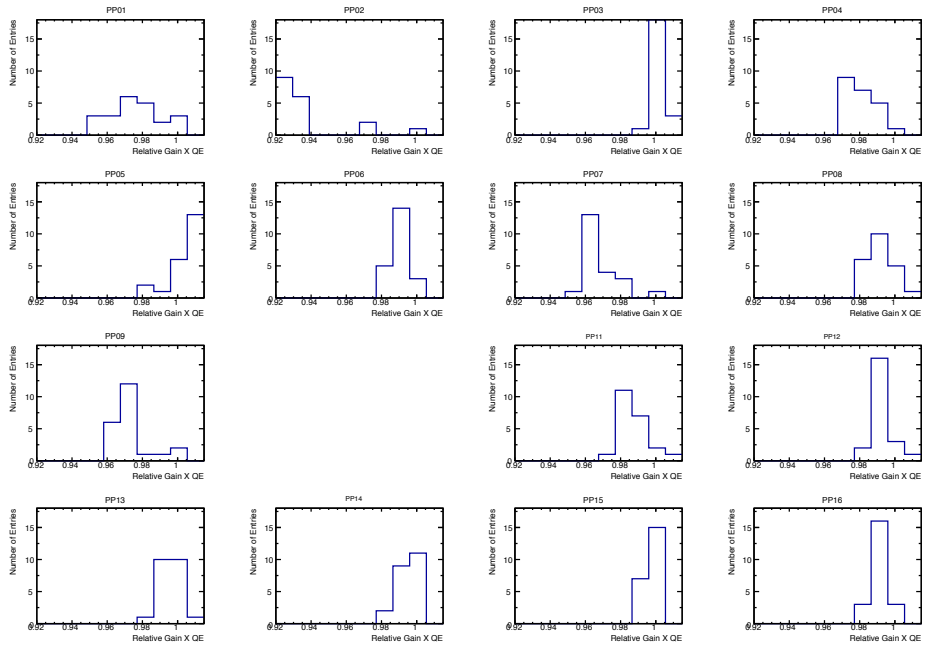

Figure 7.15: *Distribution of the gain × quantum efficiencies for all the PP after the aging was ended. PP10 is the reference PP with the modified preamp, and PP03 was the control PP that was not aged.*

Figure 7.15 shows the distribution of the product of the gain and the quantum efficiency after then aging was ended. Figure 7.16 shows the RMS of the gain × quantum efficiencies seen in figures 7.13 & 7.14 as a measure of the variability of the system, including the aging. It was found that the average relative RMS/mean was $(2.19 \pm 0.26)\%$.

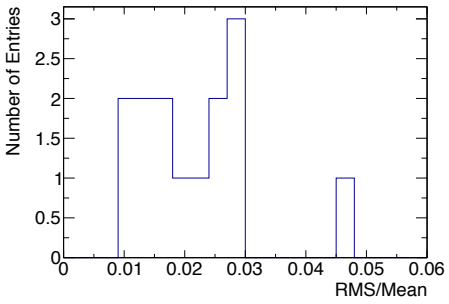

Figure 7.16: *Distribution of the RMS/mean of each PP (projection of figures 7.13 & 7.14 onto the y-axis). This distribution has an average of* $(2.19 \pm 0.26)\%$.

Comparing the variability in the control tube during the aging, the control PP had a variability (RMS/mean) of $(1.2 \pm 0.1)\%$, and after the aging was over the variability was $(0.27 \pm 0.04)\%$. It is possible that this variability is simply due to the decreased run time post-aging, however this is also probably more

representative of the variance of the PP signal.

7.4 Conclusion

Simulating usage in a 1.5 T axial magnetic field, the PP were run at an operating voltage that set the PP gain to about one third of the typical maximum [27], and were aged with a UV light source. The aging process took place over 48 days, with approximately 7 C of charge passing through the anode, equivalent to 70 years of standard Belle II operation. Over this period, the performance of the 14 tested PP was reduced to $(93 \pm 3)\%$ of the initial value. For some, most of this aging occurred during a burn-in period lasting for about 1 C, but there remains a large scatter of different behaviours among the PP. The PP performance was tracked with the use of a ^{207}Bi calibration source. With two constant visible energy deposits in the crystal, the product of the gain and quantum efficiency was found and used as a measure of the PP performance. This quantity dictates the output signal size for a given incident light intensity. There is evidence that the aging continued past the point where the light source was switched off. It is possible that the PP aging is not a function of the charge passed through the anode, but rather of some other quantity. Alternatively, there could be a delay in the aging, where the effects of the light source are offset by a delay in real time. The excess noise factor measurement, which made use of the same set of PP, was chronologically prior to the aging measurement and some burn in may have occurred then. In the measurements presented, there is no evidence of a delay at the start of the measurement. It should be noted that the control PP, which was not exposed to the light source during the aging process, experienced a net zero difference in its performance.

Of note is PP02, which experienced a large instability soon after the light source was turned off. This instability occurred over less than a week and changed by about 10% with respect to the initial value at 0 C. This most likely an outlier, with the rest of the PP having a more stable behaviour after aging. The RMS of the PP performance was on average $(2.19 \pm 0.26)\%$ with respect the mean relative gain $\times$ quantum efficiency of each PP.

Chapter 8

Conclusion

The R11283 Hamamatsu photopentode (PP) is a low gain, fine mesh photomultiplier tube intended for use in the Belle II endcap calorimeter in conjunction with pure CsI scintillation material. The design of the device optimizes performance in a high magnetic field and large anode currents.

The electronic noise was measured in two ways: using cosmic muons it was estimated to be (77 ± 2) keV, and as a side effect of measuring the excess noise factor it was found to be (32 ± 1) keV, although with a different CsI crystal. In the first case, it is thought that there may be some violated assumptions when passing the PDF to the fitting program in ROOT. In the second case, a smaller crystal of higher quality was used to determine the energy to DAQ output calibration, which is the source of the smaller equivalent noise energy. From the excess noise factor measurements, the electronic noise of the preamp was found to be equivalent to 1730 ± 33 electrons at the anode.

Using a small pure CsI crystal and a few radioactive calibration sources, the variation with temperature was found to be $(-1.65 \pm 0.02)\ \%/^{\circ}C$, and it was discovered that the time until the dynodes became thermally equilibrated was on the order of 8 to 12 hours. The PP stability after thermal equilibrium was $(0.28 \pm 0.03)\%$ for time scales on the order of a week. The PP was also found to have a linear energy response. The slope of this response, proportional to the gain $\times$ quantum efficiency, is correlated with many of the measurements Hamamatsu provides with their shipments. A summary of the values Hamamatsu measured for the set of PP used in these experiments can be found in table 5.1.

A relationship of interest to providing quality control parameters would be to correlate the change in PP performance from the aging measurement (albeit with additional statistics) with a quantity that is measurable in smaller time scales. This quantity could be any of Hamamatu's standard measurements that are currently in place, or something novel such as the excess noise factor.

The gain of the PP at an operating voltage of -1000 V was on average 255 ± 11, in stark contrast to the gain of more conventional PMTs. The

gain of the PP was also found to be linear with the operating voltage, and had an average rate of change of $(0.335 \pm 0.016)\ V^{-1}$.

A test input on the preamp was used to calibrate the DAQ. With a pulsed UV laser, the excess noise factor for the R11283 PP was found to be $(1.9 \pm 0.1 \pm 0.4)$ on average. The excess noise factor was found to vary non-linearly with the operating voltage, rising to 3.5 ± 0.1 at a gain of 25.

The lifetime of the PP was measured by inducing a current of about 2 μA though the anode by means of a UV light source. The product of the gain and the quantum efficiency was used to track the PP performance and was seen to decrease to $(93 \pm 3)\%$, when averaged over 14 devices. Fifteen of the sixteen PP were aged for 48 days, with one of the aged PPs measuring the current only, and one PP remaining unaged as a control. An integrated current of 7C was passed through the anode. This is equivalent to about 70 years of expected standard Belle II operation. Most of the aging occurred within the first coulomb of charge, however there is some evidence that there are other factors at work in the aging of the PP. The RMS, normalized by the mean of the PP performance relative to the first measurement was $(2.19 \pm 0.26)\%$ across the 14 PP.

Large scale tests of 19 stage fine mesh PMTs for the ZEUS experiment showed that the deviation in PMT performance increases as the aging progresses [32]. A similar study for the E787 experiment at Brookhaven (BNL) showed that the gain of their model smoothly drops to 85% of the initial value after 430 C, but after 10000 hours of measurement they observed that the gain returned to 100% [33]. They also observed an increase in the scatter of the PMT gain. This, with the results from figures 7.13 & 7.14 suggests that a long term study of a greater number of PP is needed to properly characterize the aging process. This is especially needed if the aging is not only dependent on the charge passing through the anode. It may be of interest to attempt to determine if there are alternate sources of aging.

While the presented study has corrected for temperature and the DAQ pedestal, there may be a real time delay to these measurements, as there was with others. For instance, it was observed that there exists a delay between immersing the PP in an environment and for the PP to reach thermal equilibrium with that environment. For the case of use in a thermally controlled area, especially if the thermal conditions greatly differ from typical room conditions, this delay would help determine the amount of dead time needed between servicing the PPs and being able to take reliable measurements. A similar delay time related to the aging may need to be characterized for the period prior to taking measurements. In case of delays on the order of an hour, one would need a new method of tracking the PP performance while

the aging is in progress, in order to compare the performance during aging and between aging sessions.

Bibliography

[1] C. Hearty, E. Ji, and P. Lu, "First Results with the Montreal Photopentode Preamp at TRIUMF." Internal notes from ECL group meeting (`http://kds.kek.jp/conferenceDisplay.py?confId=14102`), October 2013.

[2] C. Hearty, "Updated Measurements on the Performance of the Montreal Photopentode Preamplifier." Internal notes from ECL group meeting (`http://kds.kek.jp/conferenceDisplay.py?confId=14434`), December 2013.

[3] E. Rutherford, "The Scattering of α and β Particles by Matter and the Structure of the Atom," *Philosophical Magazine.*, vol. 21, pp. 669–688, 1911.

[4] Belle, A.Abashian, *et al.*, "The Belle Detector," *Nuclear Instruments and Methods in Physics Research A*, vol. 479, pp. 117–232, 2002.

[5] Belle, K.Miyabayashi, *et al.*, "Physics Achievements from the Belle Experiment," *Prog. Theory. Exp. Phys.*, 2012. DOI: 10.1093/ptep/pts072.

[6] Belle II, T.Abe, *et al.*, "Belle II Technical Design Report," 2010. arXiv:1011.0352.

[7] BABAR, B. Aubert, *et al.*, "The BABAR Detector," *Nuclear Instruments and Methods in Physics Research A*, vol. 479, pp. 1–116, February 2002.

[8] Belle, K. Abe, *et al.*, "Observation of Large *CP* Violation in the Neutral B Meson System," *Phys. Rev. Lett.*, vol. 87, p. 091802, Aug 2001.

[9] BABAR, B. Aubert, *et al.*, "Observation of *CP* Violation in the B^0 Meson System," *Phys. Rev. Lett.*, vol. 87, p. 091801, Aug 2001.

[10] Nobelprize.org, "The Nobel Prize in Physics 2008." `http://www.nobelprize.org/nobel_prizes/physics/laureates/2008/`.

[11] G. Isidori, Y. Nir, and G. Perez, "Flavor Physics Constraints for Physics Beyond the Standard Model," *Annual Review of Nuclear and Particle Science*, vol. 60, no. 1, pp. 355–380, 2010.

[12] A. Kuzmin, "Endcap Calorimeter for SuperBelle Based on Pure CsI Crystals," *Nuclear Instruments and Methods in Physics Research Section A: Accelerators, Spectrometers, Detectors and Associated Equipment*, vol. 623, no. 1, pp. 252 – 254, 2010. 1st International Conference on Technology and Instrumentation in Particle Physics.

[13] K. Miyabayashi, "Belle Electromagnetic Calorimeter," *Nuclear Instruments and Methods in Physics Research Section A: Accelerators, Spectrometers, Detectors and Associated Equipment*, vol. 494, no. 13, pp. 298 – 302, 2002. Proceedings of the 8th International Conference on Instrumentation for Colliding Beam Physics.

[14] Saint-Gobain Crystals, "CsI(pure) Cesium Iodide Scintillation Material," tech. rep., Saint-Gobain Ceramics & Plastics, Inc., 2007. Accessed August 3, 2015 at `http://www.crystals.saint-gobain.com`.

[15] Saint-Gobain Crystals, "CsI(Tl), CsI(Na) Cesium Iodide Scintillation Material," tech. rep., Saint-Gobain Ceramics & Plastics, Inc., 2007. Accessed August 3, 2015 at `http://www.crystals.saint-gobain.com`.

[16] C. Amsler, D. Grgler, W. Joffrain, D. Lindelf, M. Marchesotti, P. Niederberger, H. Pruys, C. Regenfus, P. Riedler, and A. Rotondi, "Temperature Dependence of Pure CsI: Scintillation Light Yield and Decay Time," *Nuclear Instruments and Methods in Physics Research Section A: Accelerators, Spectrometers, Detectors and Associated Equipment*, vol. 480, no. 23, pp. 494 – 500, 2002.

[17] Belle II Collaboration, "Belle II Wireframe." `http://belle2.kek.jp/images/BelleII-outline.pdf`. Image altered. Photo accessed May 11, 2015.

[18] J. Haba, "Letter of Intent for KEK Super B Factory, Part II: Detector," April 2004. `https://belle2.cc.kek.jp`.

[19] PANDA, A.Borisevich, *et al.*, "PWO-II Scintillation Crystals for the PANDA Electromagnetic Calorimeter," in *IEEE Nuclear Science Symposium Conference Record*, pp. 2698–2700, 2008.

[20] B. Shwartz, "Belle Calorimeter Upgrade," *Nuclear Instruments and Methods in Physics Research Section A: Accelerators, Spectrometers, Detectors and Associated Equipment*, vol. 598, no. 1, pp. 220 – 223, 2009. Instrumentation for Collding Beam Physics Proceedings of the 10th International Conference on Instrumentation for Colliding Beam Physics.

[21] Hamamatsu Photonics K.K., "Photomultiplier Tubes: Basics and Applications," 2007.

[22] Hamamatsu Photonics K.K. Electron Tube Division, "Photomultiplier Tube R11283 Technical Data," tech. rep., Hamamatsu Photonics, April 2013.

[23] J.-P. Martin, N. Starinski, and P. Taras, "Fast Charge-sensitive Preamplifier for Pure CsI Crystals," *Nuclear Instruments and Methods in Physics Research Section A: Accelerators, Spectrometers, Detectors and Associated Equipment*, vol. 778, pp. 120 – 125, 2015.

[24] A. Hershenhorn, "CsI Cosmic Muon Deposit Energy." Private communication.

[25] S. Ritt *et al.*, "Maximum Integrated Data Acquisition System," 1993-. `https://midas.triumf.ca`.

[26] M. W. Davidson, "Tungsten-Halogen Incandescent Lamps." Accessed August 13, 2015. `http://zeiss-campus.magnet.fsu.edu/articles/lightsources/tungstenhalogen.html`.

[27] A. Kuzmin, "Endcap Calorimeter for SuperBelle based on Pure CsI Crystals," *Nuclear Instruments and Methods in Physics Research Section A: Accelerators, Spectrometers, Detectors and Associated Equipment*, vol. 623, no. 1, pp. 252 – 254, 2010. 1st International Conference on Technology and Instrumentation in Particle Physics.

[28] A. Karar, Y. Musienko, and J. Vanel, "Characterization of Avalanche Photodiodes for Calorimetry Applications," *Nuclear Instruments and Methods in Physics Research Section A: Accelerators, Spectrometers, Detectors and Associated Equipment*, vol. 428, no. 23, pp. 413 – 431, 1999.

[29] Y. Jin, H. Aihara, O. Borshchev, D. Epifanov, S. Ponomarenko, and N. Surin, "Study of a Pure CsI Crystal Readout by APD for Belle II

End Cap ECL Upgrade," *Nuclear Instruments and Methods in Physics Research Section A: Accelerators, Spectrometers, Detectors and Associated Equipment*, pp. –, 2015.

[30] S. de Jong, "ECL backgrounds in the 11th campaign," in *21st Belle 2 General Meeting*, 2015.

[31] C. Hearty, "Initial Studies with SICCAS CsI Crystal and Preamp V3." Internal notes from ECL group meeting, April 2014.

[32] T. o. Ishii, "Automatic Test of Photomultiplier Tubes for the ZEUS Forward and Rear Calorimeters," *Nuclear Instruments and Methods in Physics Research A*, vol. 320, pp. 449–459, Jan 1992.

[33] T. K. Komatsubara *et al.*, "Performance of Fine-mesh Photomultiplier Tubes Designed for an Undoped-CsI Endcap Photon Detector," *Nuclear Instruments and Methods in Physics Research A*, vol. 404, pp. 315–326, Feb. 1998.

[34] Teledyne LeCroy, "Modular ADCs for Physics and Chemistry." Accessed August 12, 2015. `http://teledynelecroy.com/lrs/dsheets/2249.htm`.

[35] Saint-Gobain Crystals, "Detector Assembly Materials," tech. rep., Saint-Gobain Ceramics & Plastics, Inc, 2005. `http://www.crystals.saint-gobain.com/uploadedFiles/SG-Crystals/Documents/Organic%20Product%20Accessories%20Data%20Sheet.pdf`.

[36] Momentive Perfomance Materials, "TSE3032 Technical Data Sheet," tech. rep., Momentive Perfomance Materials, 2015. Acessed 08/07/15. `https://www.momentive.com/products/showtechnicaldatasheet.aspx?id=10404`.

[37] Hamamatsu Photonics K.K., "R5113-02 Photomultiplier Tube Data Sheet." Accessed Aug 10, 2015 at `http://www.hamamatsu.com/jp/en/R5113-02.html`.

[38] R. B. Firestone, "The Berkeley Laboratory Isotopes Project's Exploring the Table of Isotopes," May 2000. Accessed on August 13, 2015. `http://ie.lbl.gov/education/isotopes.htm`.

[39] H. Ikeda *et al.*, "A Detailed Test of the CsI(Tl) Calorimeter for BELLE with Photon Beams of Energy Between 20 MeV and 5.4 GeV," *Nuclear*

Instruments and Methods in Physics Research Section A: Accelerators, Spectrometers, Detectors and Associated Equipment, vol. 441, no. 3, pp. 401 – 426, 2000.

Appendix A

Circuit Diagrams

A.1 Electronic Noise

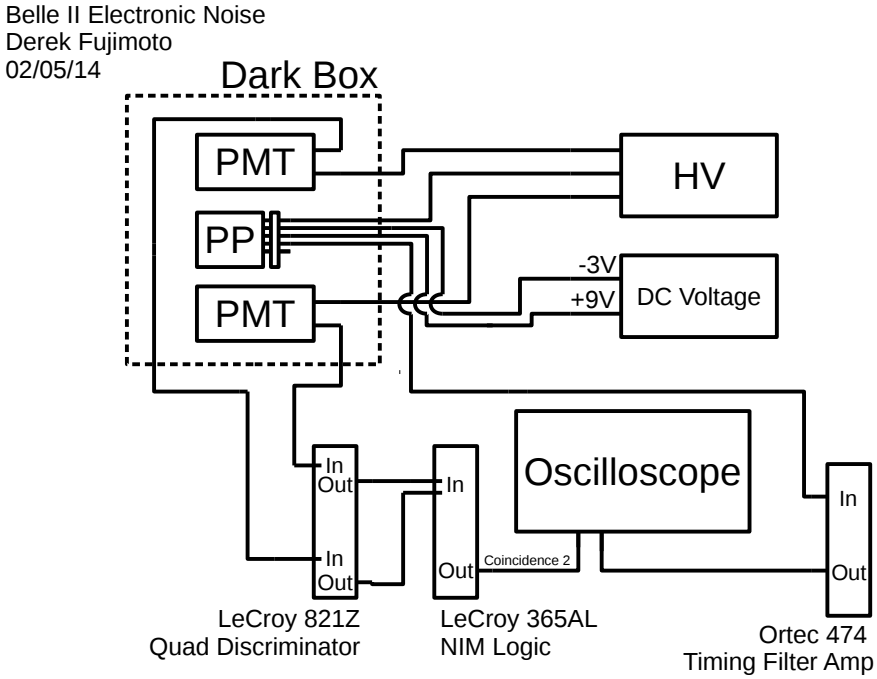

Figure A.1: *Circuit diagram for the electronic noise measurement in chapter 3.*

A.2 Short Term Stability

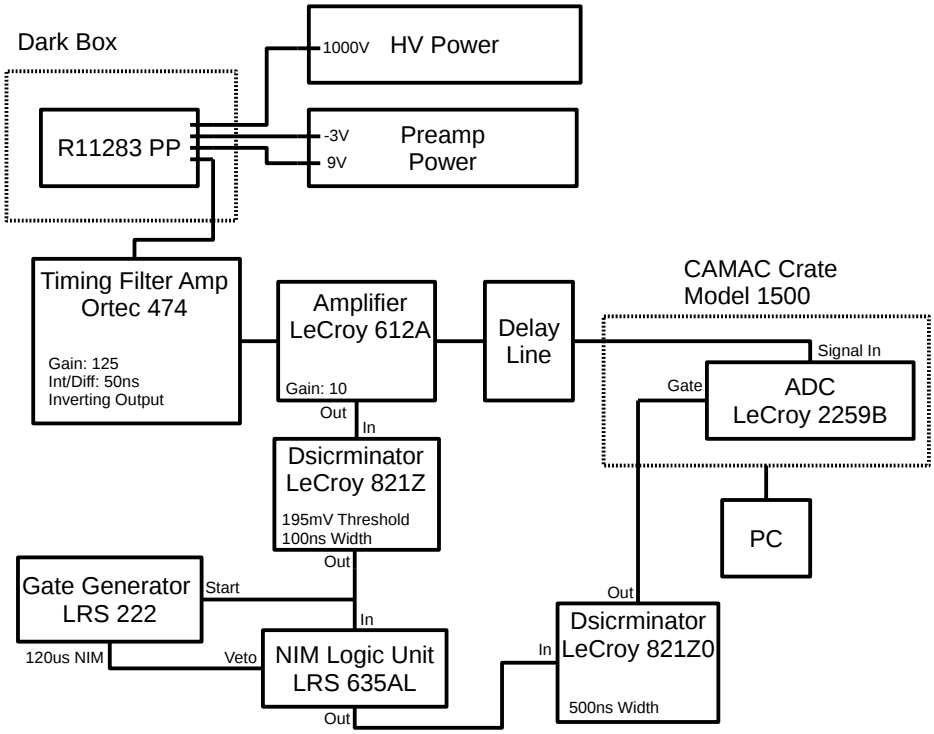

Figure A.2: *Circuit diagram for the short term stability measurement in chapter 4.*

A.3 Excess Noise Factor

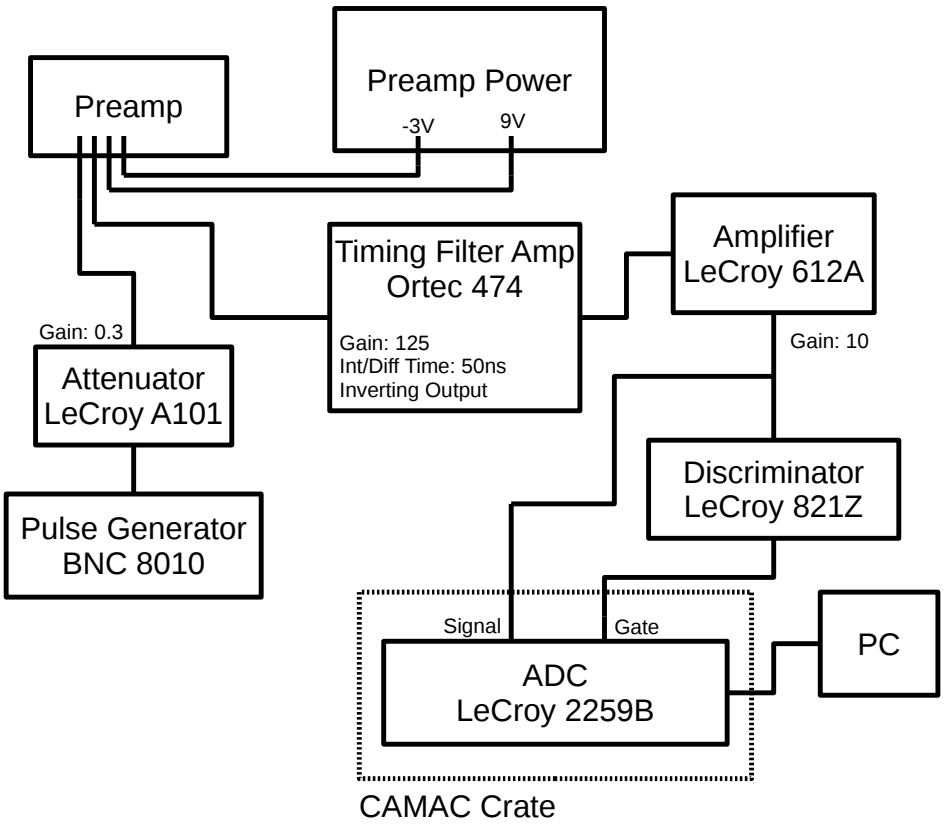

Figure A.3: *Circuit diagram for the calibration pulse measurement in chapter 6.*

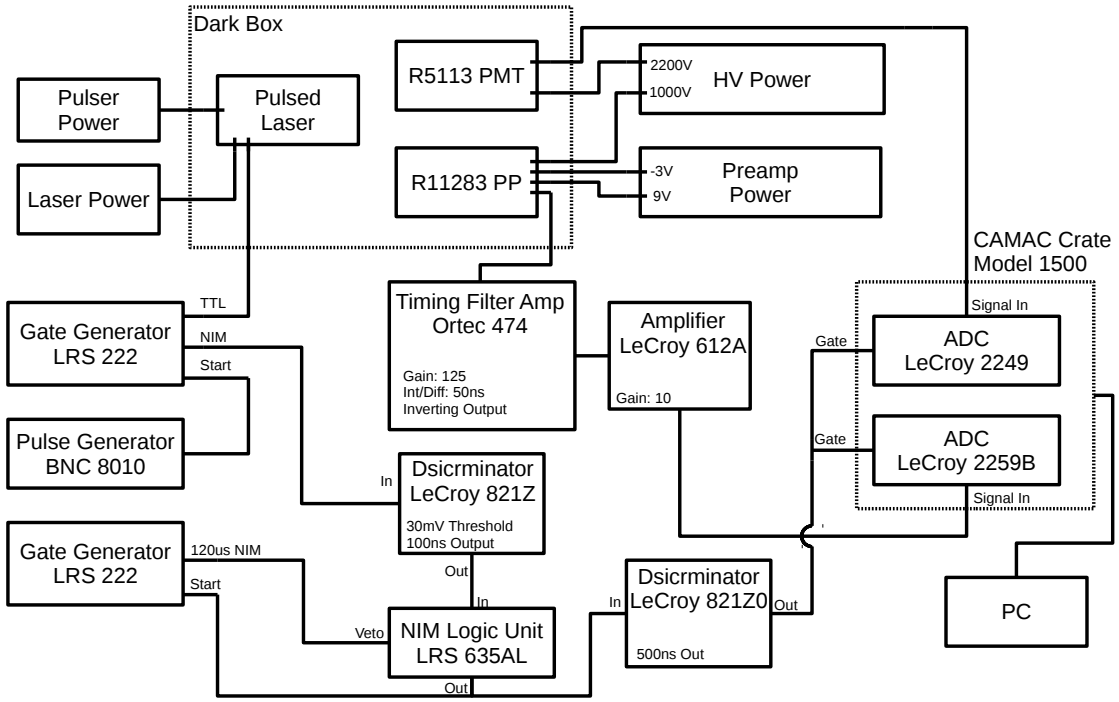

Figure A.4: *Circuit diagram for the excess noise factor measurement in chapter 6.*

A.4 Aging and Lifetime

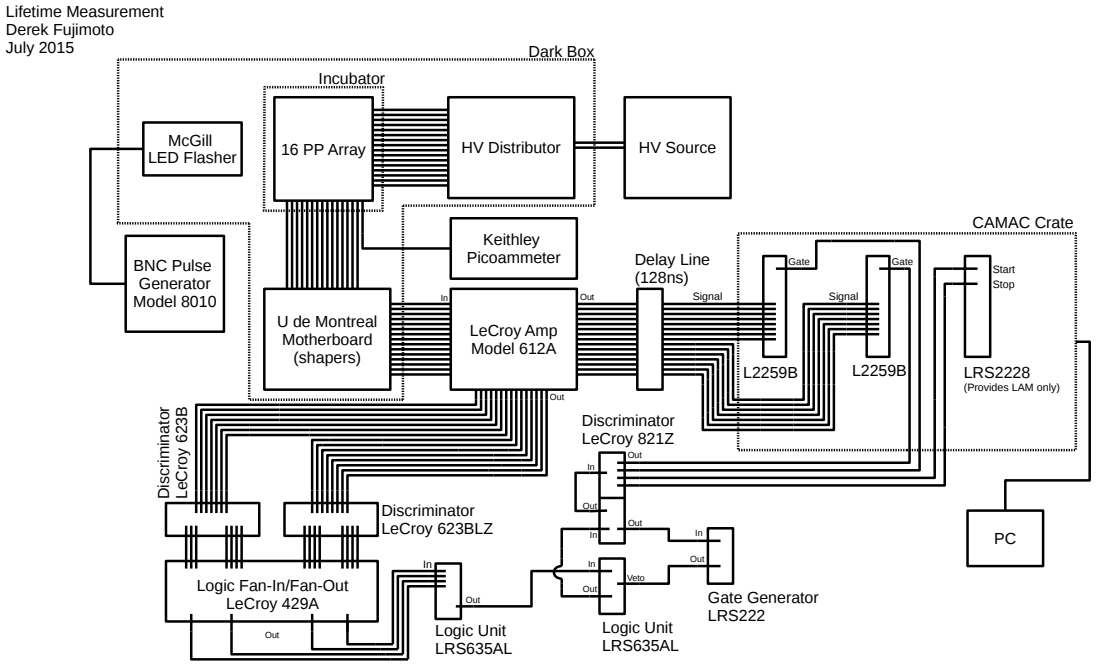

Figure A.5: *Circuit diagram for the aging and lifetime measurement in chapter 7.*

Appendix B

Equipment Specifications

B.1 Electronics

B.1.1 U. de Montréal Preamp V3

The purpose of the preamp is to produce a step function whose amplitude is proportional to the integrated current passing through the anode over a given time. This step function is sent to a shaper that produces a signal whose amplitude is proportional to the amplitude of the preamp output. What is generally referred to in the main body of this work as "the preamp" is the printed circuit board housing both the voltage divider and the preamp circuit. Version 3 of this board can be seen in figure 2.3. The board has six soldered cables: two voltage inputs to power the preamp circuit, one high voltage (HV) input for the voltage divider, a signal out cable, a calibration test pulse input, and a ground strap.

The preamp power inputs were set to +9 V and -3 V and were connected to an external DC power supply.

The HV input goes directly to the high voltage divider. This circuit (fig. B.1) is isolated from the preamp circuit and distributes the correct amount of voltage to the photocathode, dynodes, and the anode of the PP.

The calibration test pulse input leads to a (1 ± 0.25) pF capacitor, which allows for the injection of a known amount of charge into the preamp. The

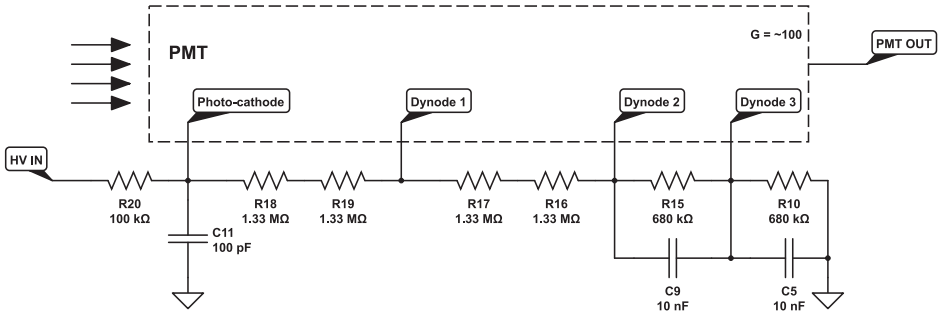

Figure B.1: *Université de Montréal voltage divider [23].*

preamp then processes this charge as if it were a real signal. This is useful for calibrating the readout electronics and for determining corresponding the number of electrons from the shaper.

The preamp ground strap was clamped to a larger ground strap, which often served as the ground for the dark box as well. This ground strap was ultimately connected to the building's electrical ground, through the NIM crate.

The preamp and voltage divider are connected to the PP via five flying leads, which are inserted through the board. The ends of the flying leads were covered in electrical heat shrink to prevent sparking, which was otherwise a significant source of noise.

B.1.2 U. de Montréal Preamp V4 and Motherboards

Version 4 of the preamp (fig. B.2) did not have many functional changes from V3 [23]. The primary change was the inclusion of a mini-display port cable to carry the -3 V and +9 V voltages, the signal out, the calibration pulse signal, and the ground to the preamp. The HV cable was updated to

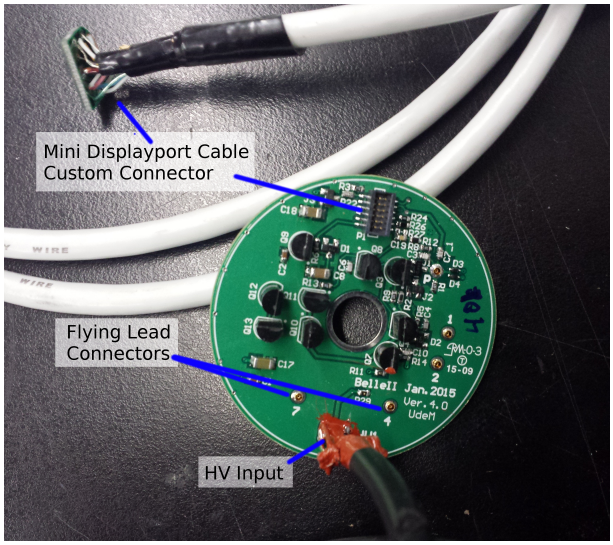

Figure B.2: *Université de Montréal V4 preamp.*

a SHV cable, eliminating the need for an adapter. The mini-display port cables were connected to a motherboard (fig. B.3) which housed the shapers and distributed power to the preamps. The motherboard is powered by four DC voltages: ±12 V and ±6 V via a DB9 connector, and has a separate

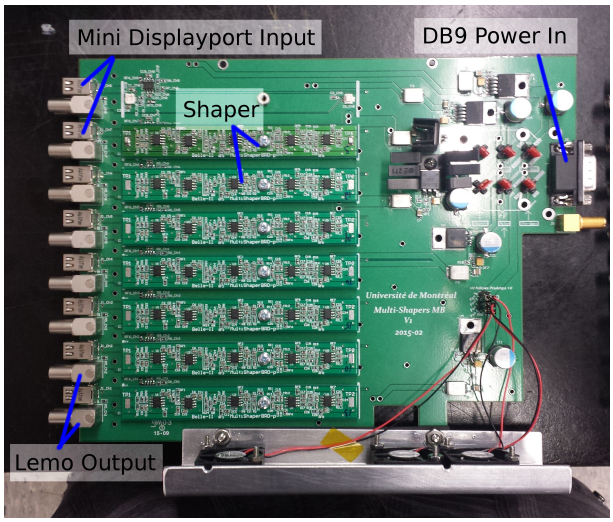

Figure B.3: *Université de Montréal motherboard and shapers.*

input for the calibration pulse. Each motherboard contains housing for 8 shapers, which are removable. The signal output of the shapers are lemo connectors.

There were a few issues when using the mini-display port cables. The cables were single sided: only one end of the cable had the standard connector, whereas the other end had a custom port to connect to the preamp. The custom end of the cable was extremely fragile, and was easily damaged. Additionally, this end pulled out of the preamp socket quite easily, rendering any usage with an inaccessible preamp difficult. The other end of the cable worked extremely well. For future iterations of the preamp, it would be best to keep the standard connector on both ends of the mini-display port cables. In this way, the cables can be exchanged with others, in the case where there is damage or a cable of a different length is needed. This would also provide a more secure connection to the preamp.

The primary issue with the motherboards was signal pickup from the DB9 power input. This was because the cables initially used were not coaxial. The solution was to solder lemo cable connectors to the ends of the DB9 inputs, and to install lemo feedthroughs in the dark box. Since the motherboards were encased in the shielded dark box, this reduced pickup immensely.

B.1.3 Modifed Preamp

With the V4 preamps, U. de Montréal also included a modifed preamp (fig. B.4) which allowed for the direct reading of current from the anode of the PP. This was specifically designed for use with the Keithley 6485 Picoammeter. For the most part the modified preamp performed well, with the exception of a weak mechanical connection between the resistors and the printed board. The modified preamp does not house the preamp electronics present in the other preamps and did not allow for the readout of signals in the same manner.

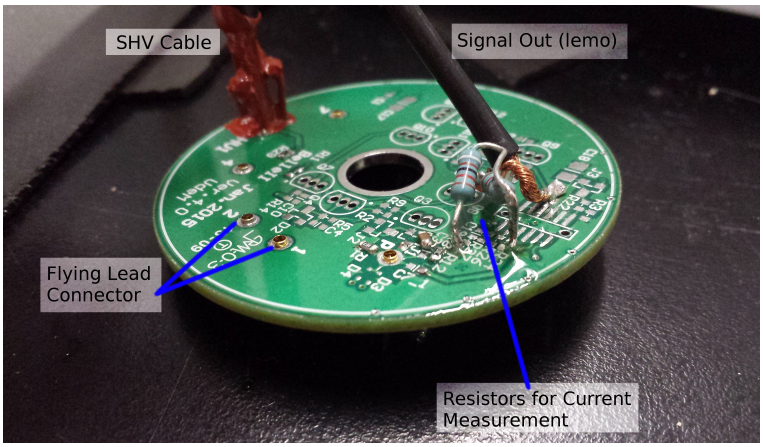

Figure B.4: *Université de Montréal modified preamp for reading current.*

The modified preamp current output was measured as a function of the PP operating voltage, to convert the baseline measurements to the proper values. This is seen in figure B.5 with a linear fit. The current was averaged over a period of 5 minutes.

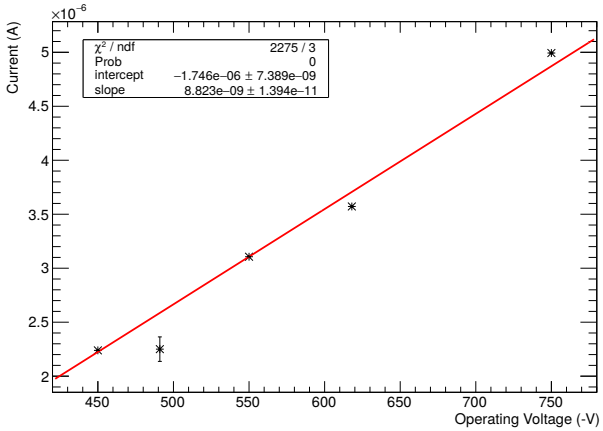

Figure B.5: *Current from the modified preamp, connected to the control PP, as a function of operating voltage, with linear fit.*

B.1.4 LeCroy L2249 and L2259B

Two LeCroy ADCs were used in conjunction with the CAMAC crate and the MIDAS DAQ software: the L2259B peak sensing ADC to measure the shaper output on signals from the PP, and the L2249 integrating ADC to measure output from a standard PMT. The standard PMT used in this experiment was the Hamamatsu R5113-02. Despite their differences in functionality, the ADCs are very similar in design. Each is a 12-channel single slot NIM unit with a test input and gate, and have many of the same design specifications [34]. The L2259B accepts inputs from 0 V to −2 V with rise times longer than 50 ns. The rise time was discovered to be an important requirement for in-going signals. If the gate start was within 50 ns of the peak, the ADC failed to find the proper amplitude for the signal. The L2259B also has a 106 μs digitization time, which is why the circuits were designed to generate 120 μs of dead time between signals. Additionally, as seen in figure B.6, the ADC output was non-linear for small pulses. In contrast, it was found that the L2249 ADC was linear over its full range.

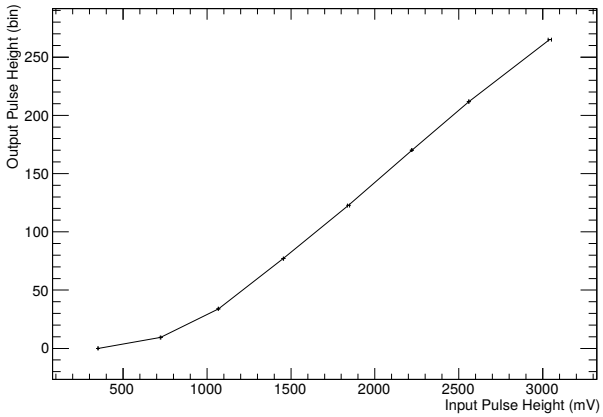

Figure B.6: *The L2259B LeCroy ADC is nonlinear for input pulses scoring below bin 50. The measured pulse is the output of the calibration test pulse from the preamp. The x-axis is the calibration pulse input voltage.*

B.2 Optics

B.2.1 Optical Grease

The optical grease used was the BC-630 Silicone Grease manufactured by Saint-Gobain. This model of grease has a 95% optical transmission for wavelengths between 280 nm and 700 nm. However, the transmission drops to nearly zero below 270 nm. The grease has an index of refraction of 1.465 and has low evaporation at room temperature [35]. Recall that the light produced by the scintillation of CsI peaks at 315 nm, making this optical grease a good candidate for the optical connection.

It was observed that the grease formed a light mechanical connection between the crystal and the PP. However, if a large amount of grease was used, the light yield read out by the PP was diminished. Additionally, after some time the grease would react with the CsI and become slightly yellowed. The grease had to be renewed every few weeks to maintain a high quality optical connection.

B.2.2 Silicone Rubber

To glue to PP to the CsI crystals, a two part transparent silicone rubber was used. This rubber was produced by Momentive Performance Materials, and has the product number TSE3032(A) and TSE3032(B). The

rubber cures when the two types are mixed. TSE3032 has a refraction index of 1.406 and a nominal mixing ratio of 100:10 (A:B) by weight [36]. The mixing procedure is as follows:

- Weigh a given amount of TSE3032(A).
- Add 10% of TSE3032(B).
- Mix carefully.
- Place mixture in a vacuum until air bubbles have vanished.

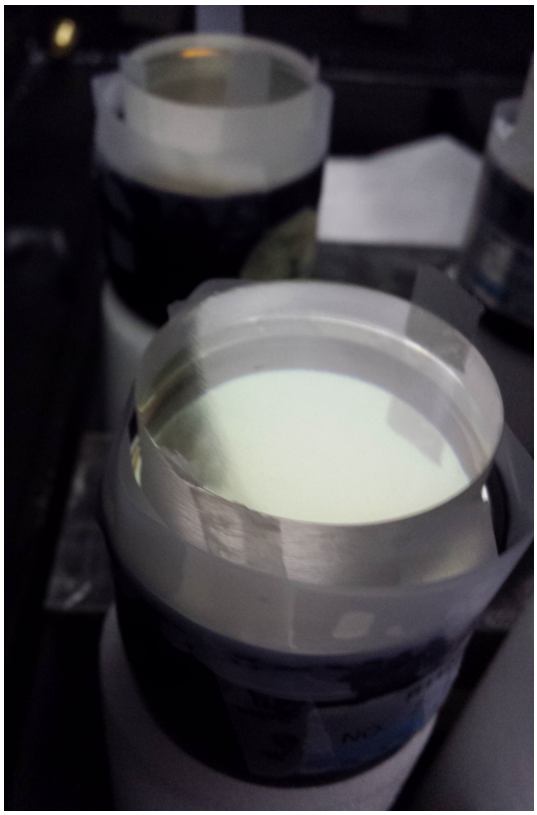

Figure B.7: *CsI crystal being glued to the PP using TSE3032. The tape is to prevent the crystal sliding off of the PP while it was drying.*

To glue the CsI to the PP, the PP was clamped such that the face of the PP was upwards and level, as in figure B.7. The mixed TSE3032 was added carefully to the center of the PP face. The CsI was then slowly pressed onto the glue, with one edge down first, such that the glue only made initial contact at one point with the crystal. The face of the CsI was then eased down until the whole face was pressed onto the PP. The contact was then inspected: if there were any air bubbles or if the silicone rubber did not cover the whole face, the CsI was removed, both surfaces were wiped down, and the process was restarted.

Since the silicone rubber was quite viscous prior to being cured, the CsI was lightly taped down along the sides to hold it in place. As an additional safety measure, a "fence" of tape was applied around the edges of the PP to ensure that the CsI did not fall off the PP in the case the aforementioned tape did not hold. This setup was left to cure overnight.

B.2.3 Standard High-Precision PMT

The standard, high-precision, PMT used was the Hamamatsu R5113-02 photomultiplier tube [37]. It has similar characteristics as the R11283 photopen-

tode of chapter 2. It is a head-on type, with a 51 mm diameter window made of UV glass. It is sensitive to light with wavelength in the range of 185 nm to 650 nm, peaking at 420 nm. It has a bialkali photocathode, and 12 dynode stages in a linear structure. The gain of the particular tube used, with the output being attenuated by a factor of 0.3, was $(3.99 \pm 0.15) \times 10^6$, as detailed in section 6.3.1.

B.2.4 Pulsed UV Laser

The pulsed UV laser used in the excess noise experiment of chapter 6 was a custom device constructed by Pierre Amaudruz of the TRIUMF DAQ group. The output wavelength of the light was 405 nm which was transmitted along the length of a fibre optic into the dark box. The pulser was run by two power sources, one of which set the intensity of the light emitted. The laser pulses were triggered by a TTL logic signal, which was sent from a NIM pulse generator.

The fibre optic used was the HPSC25 from thorlab.com, and has a numerical aperture of 0.100 ± 0.015. The numerical aperture describes the angles over which the system can accept or emit light. It is given by

$$NA = n \sin(\theta), \tag{B.1}$$

where NA is the numerical aperture, n is the index of refraction in the medium in which the system is contained, and θ is the angle of acceptance or emittance. Using $n = 1$ for air, means that the light exiting the fibre optic is emitted at an angle no greater than $\theta = 0.100 \pm 0.0015$ radians. Therefore the radius of the illuminated portion of the screen is one-tenth the screen to laser distance. The largest screen to laser separation used was 60 cm, therefore since the reflective screen was wider than 12 cm, all of the light was reflected off, or absorbed by the black floor of the dark box.

B.2.5 Diffuse Reflective Screen

Seen in figure B.8, a diffuse reflective screen was used to provide uniform light to the PP and the standard PMT. This screen reflected the laser light provided by the pulsed UV laser in appendix B.2.4. There were several materials tested including: printer paper (new and yellowed), sandpaper of three different grits and colours, and mylar copy paper. The copy paper was a semi-transparent tracing paper used to copy blueprints. One side of the paper provided diffuse reflections while the other produced primarily specular reflections. The final screen design was four layers of the mylar copy paper taped around the edges on a G10 board, with the diffuse side outwards. Since both the G10 board and the copy paper were slightly transparent, a layer of fine grit sandpaper was used behind the board to provide a neutral background. Tape was required around the edges since the mylar picked up a lot of dust and became dirty quickly. Care was taken to ensure that the lower layers of mylar were clean before being taped. The whole setup was 18 cm $\times$ 28 cm and taped to an aluminum support structure so that it remained upright and perpendicular to the PP.

Figure B.8: *Diffuse reflective screen used in excess noise measurements of chapter 6.*

B.2.6 McGill LED Array

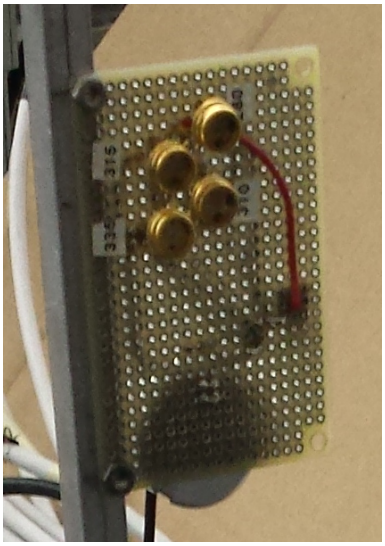

Figure B.9: *LED array designed to produce light that emulates the emission spectrum of CsI. Designed and produced at McGill University.*

An LED array (fig. B.9) was designed and constructed by Amiel Kollek of McGill University, with light output closely matching the wavelength of maximum emittance of CsI. The array was composed of four UV LEDs emitting light of 335 nm, 315 nm, 310 nm, and 280 nm. These were set in parallel with each other and in series with a variable resistor so that larger voltages may be used. The array was supposed to deliver an amount of light to the PP that was comparable to a CsI signal, but at a much higher rate in order to age the PP. It was observed that three of the four LEDs had experienced a catastrophic failure and were irreparably damaged. This probably occurred during the search for a suitable pulse generator to run the LEDs, as the model used at McGill was not readily available at TRIUMF. With the remaining LED (335 nm), the array was run with a DC power source with signals reaching the PP at a rate of about 1 MHz.

The LEDs were produced by SETi (Sensor Electronic Technology, Inc.) model number UVTOP***TO39FW, where *** corresponds to the four wavelengths stated above. They are a flat window type with a typical FWHM of 10 nm. The typical forward voltage of the LED is 5.5 V, with optical power of 600 μW.

B.3 Miscellaneous Equipment

B.3.1 Dark Box

For all of the measurements presented in this work, the experimental setup was encased in a dark box (fig. B.10). The purpose of the dark box was threefold: to create a low light environment where the photomultiplier tubes

could be operated safely, to shield from electromagnetic interference, and to provide a low humidity environment for the CsI. For the first few trials of the electronic noise measurement, the dark box left over from Eddie Ji and Christopher Hearty was used. However due to foreseen space constraints, a larger box was soon purchased and light-proofed by Chelsea Dunning. The light proofing was done with the standard PMT and a optically opaque tape. The dark box itself was made of steel with interior dimensions of about 43.5 cm in height, 43 cm to 49.5 cm in width, and 119.5 cm in length. A layer of foam was taped around the open edge of the box, such that it was compressed when the lid was shut, and the latches were taped over to ensure light-tightness.

Figure B.10: *The dark box, prepared by Chelsea Dunning, that was used for all but the most preliminary measurements.*

The box was also grounded with a ground strap. The paint in a small area on the lid and body of the box was sanded off and bolts with wingnuts were installed to clamp the ground strap to both the body and the lid. On the inside, another ground strap was clamped to the body in the same manner, such that the box remained light-tight while allowing the electronics inside to be grounded properly. The grounding of the box played a significant role in reducing noise from pickup. Feedthroughs were installed for all necessary cables, except for the humidity and temperature probe, which was not readily detachable from the main device.

B.3.2 Desiccant

To keep the humidity low, desiccant was used to absorb water from the air. Two types of desiccant were used: clay and a molecular sieve. As reported

by Chelsea Dunning, the molecular sieve was more effective at reducing the humidity than the clay type. The molecular sieve also had the advantage that it could be regenerated. This was performed by placing a tin of the desiccant in an oven at 160 °C overnight, while flushing the oven with N_2 gas. Initially, a vacuum pump was used in place of the gas, but this idea was retired after the vacuum was nearly damaged from water condensing out of the air while in the pump. The sieve used had a 4 Å pore size and was of the pellet type produced by Advanced Specialty Gas Equipment (ASGE).

B.3.3 BINP CsI Crystal

For the electronic noise measurements presented in chapter 3, a pure CsI crystal on loan from the Budker Institute of Nuclear Physics (BINP) was used. As with the Belle crystals, this one was wrapped in a Gore-Tex film and covered with aluminized mylar. It was a truncated pyramid with a cross section of approximately 6 cm × 6 cm at the large end, 5.4 cm × 5.4 cm at the narrow end, and about 30 cm in length. The PP was always connected to the larger end of the crystal.

As with all pure CsI, this crystal was kept in a low humidity environment to prevent damage to the crystal surface.

B.3.4 Temperature and Humidity Probe

As seen in figure B.11, the HH314A Temperature and Humidity Meter by Omega Engineering was used for measurements in the dark box. This probe came with software that could be used to monitor and record the temperature and humidity at set time intervals via a computer. The precision of the temperature measurements was 0.1 °C.

Figure B.11: *Temperature and humidity reader base for measurements within the dark box.*

B.3.5 Incubator

The incubator used was the 10-140 General Incubator produced by Quincy Labs, with interior dimensions 31×25×25 cm (fig. B.12). It is a heating-only

type, therefore the set temperature needed to be larger than the ambient temperature to ensure a stable environment.

For the aging measurement, the standard window was replaced with a UVT acrylic window so that the UV LED light would age the PP properly. Additionally, the rear wall of the incubator was converted into a sliding panel, so that the preamps and mini displayport cable connections could be accessed. There was a small hole cut into the panel to let the SHV and mini displayport cables out of the incubator.

Figure B.12: *Incubator used in experimental setup. Version shown has UVT window installed, and contains mechanical support structure for the aging measurements in chapter 7.*

B.3.6 Calibration Sources

Three calibration sources were used: ^{137}Cs ^{22}Na and ^{207}Bi . Below is a table of the energies of the common decays that produce gammas:

Table B.1: *Calibration source decay energies in keV [38]. Note that the 511 keV decay from the ^{22}Na source is from positron annihilation and is not due to a ^{22}Na gamma.*

^{137}Cs	^{22}Na	^{207}Bi
661.657	511.006	569.702
	1274.53	1063.662
		1770.237

Appendix C

Functions

C.1 Novosibirsk

As described in reference [39], the Novosibirsk function is given by

$$F(x; N, x_p, \sigma_E, \eta) = N \ \exp\left(-\frac{1}{2\sigma_o^2}\ln^2\left(1 - \frac{x - x_p}{\sigma_E}\eta\right) - \frac{\sigma_o^2}{2}\right), \qquad \text{(C.1)}$$

where

$$\sigma_o = \left(\frac{2}{\eta}\right)\sinh^{-1}\left(\frac{\eta\xi}{2}\right)$$

and

$$\xi = 2\sqrt{\ln 4} = 2.36.$$

The variable parameters are as follows:

- N: normalization factor
- x_p: peak location
- σ_E: resolution, defined as the FWHM/ξ
- η: asymmetry parameter

The Novosibirsk function is the result of the convolution of the energy spectrum of a Compton scattered photon and a log-normal distribution. The theoretical Compton energy spectrum is given by

$$F(E_\gamma) = N\left(\left(E_\gamma - \frac{E_c}{2}\right)^2 + \frac{E_c^2}{4}\right) \qquad \text{(C.2)}$$

where E_γ is the energy of the Compton scattered photon and E_c is the Compton edge energy.

In essence, the Novosibirsk function is a asymmetric semi-infinite Gaussian function.

C.2 Excess Noise Factor

Starting from the definition of the excess noise factor in chapter 6:

$$\left(\frac{\sigma_c}{N_c}\right)^2 F = \left(\frac{\sigma_a}{N_a}\right)^2, \tag{6.1}$$

it was noted that N_c, the number of electrons at the photocathode (photoelectrons), is proportional to the number of photons incident on the photocathode by a factor corresponding to the quantum efficiency. Therefore, the photoelectrons are Poisson distributed and $\sigma_c^2 = N_c$:

$$\frac{F}{N_c} = \frac{\sigma_a^2}{N_a^2}. \tag{C.3}$$

If the internal gain of the PP is given by M, then $N_a = M \cdot N_c$. Equation C.3 does not take the electronic noise (σ_o) into account. The width of the distribution actually measured is given by $\sigma_m^2 = \sigma_o^2 + \sigma_a^2$, and the peak location is unchanged: $N_a = N_m$. Substituting all of the above into equation C.3:

$$\sigma_m^2 = (FM^2)N_c + \sigma_o^2.$$

Where σ_m and σ_o are in units of number of electrons at the anode, and N_c is in units of number of photoelectrons. Furthermore, note that since $\sigma_{m,s}$ is measured in number of electrons at the anode, then $\sigma_{m,s}/M$ is in units of photoelectrons. Therefore,

$$\sigma_{m^{pe}}^2 = F \cdot N_c + \sigma_{o^{pe}}^2, \tag{6.2}$$

where $\sigma_{m^{pe},o^{pe}}$ are in units of number of photoelectrons. Since the excess noise factor (F), the internal PP gain (M), and the electronic noise (σ_o) are all constants, equation 6.2 is a simple linear relationship. For clarity, equation 6.2 has been written in chapter 6 without the photoelectron indicators.

C.3 Excess Noise Factor: Why the PMT Was Not Useful

In chapter 6 it was stated that the original plan was to use a high precision PMT to measure the number of incident photons and to use this information to determine the excess noise factor of the PP. Since the standard PMT was able to measure single photons, a direct measurement of the PMT gain was possible, whereas the PP gain was not high enough to measure single

photons. The issue with only using the PP was that it relies on using the gain as measured by Hamamatsu, which could not be checked with the existing setup. What follows is the reasoning for why the high precision PMT was not useful, despite its significant advantage.

Recall that the excess noise factor is given by:

$$\frac{F}{N_{pe}} = \frac{\sigma_a^2}{N_a^2}, \tag{C.3}$$

where $N_{pe} = N_c$ is the number of photoelectrons. Rearranging,

$$F = N_{pe} \cdot \left(\frac{\sigma_a^2}{N_a^2} \right),$$

and since σ_a and N_a are known via direct measurement from the ADC, it follows that there needs to be a measurement of N_{pe}.

C.3.1 Method 1: The Direct Measurement of N_{pe}

To do this, note also the two following relationships:

$$N_{pe} = Q_E N_\gamma \qquad \text{(C.4)} \qquad\qquad N_{pe} = \frac{N_a}{M} \qquad \text{(C.5)}$$

where Q_E is the quantum efficiency, N_γ is the number of incident photons, N_a is the number of electrons at the anode, and M is the gain of the phototube. With the setup described in chapter 6.2, there are two ways to measure N_{pe}:

- Eqn C.4: N_γ is measured and Q_E is applied ("through the front").
- Eqn C.5: N_a is measured and M is applied ("through the back").

For the photopentode:

- Both N_γ and Q_E are unknown, thus equation C.4 is not so useful.
- N_a is measurable, but M is known only from the Hamamatsu data sheet, making equation C.5 useful but undesirable.

So a direct measurement of N_{pe} using the PP would have to apply the gain as measured by Hamamatsu, with no way of checking this value.

C.3.2 Method 2: An Alternate Expression for N_{pe}

The alternative to the direct measurement is to find an alternate expression for the N_{pe}. Equation C.5 should not be used since any use of this relationship would reduce the alternate expression back to the direct measurement case.

It is useful to know that N_γ, although unknown, can be made the same for both the PMT and the PP. This is because the setup allows for the two phototubes to be exchanged reliably, so if the signal from both phototubes does not change significantly upon exchange, it is reasonable to conclude that N_γ has not changed at either position. Using this with equation C.4:

$$\frac{N_{pe}}{\tilde{N}_{pe}} = \frac{Q_E N_\gamma}{\tilde{Q}_E N_\gamma} = \frac{Q_E}{\tilde{Q}_E} \quad \rightarrow \quad N_{pe} = \tilde{N}_{pe}\frac{Q_E}{\tilde{Q}_E} \tag{C.6}$$

where the quantities with the tilde are measured with the standard PMT, and those without by the PP. Substituting equation C.6 into equation C.3 gives

$$F = \tilde{N}_{pe} \cdot \left(\frac{Q_E}{\tilde{Q}_E}\right) \cdot \left(\frac{\sigma_a^2}{N_a^2}\right)$$

$$F \cdot \left(\frac{\tilde{Q}_E}{Q_E}\right) = \tilde{N}_{pe} \cdot \left(\frac{\sigma_a^2}{N_a^2}\right) \tag{C.7}$$

where the excess noise factor is now known up to a constant multiplier. However, as was noted earlier, Q_E is unknown, and $\tilde{Q}_E$ is unknown as well.

C.3.3 Conclusion: PMT Not Useful

The two methods for solving for the excess noise factor are then

$$F = \left(\frac{N_a}{M}\right) \cdot \left(\frac{\sigma_a^2}{N_a^2}\right) \quad \text{or} \quad F \cdot \left(\frac{\tilde{Q}_E}{Q_E}\right) = \tilde{N}_{pe} \cdot \left(\frac{\sigma_a^2}{N_a^2}\right)$$

where either the standard PMT is not useful (left) or the excess noise factor can only be found to a multiplicative constant (right). It was decided to simply make the direct measurement of N_{pe} since this used only one PP, and had less room for error. As long as the Hamamatsu measurement of the gain of the phototube is accurate, method 1 should be viable. This was why the standard PMT was included in all of the setup and procedure design, but the data from that PMT was not used to calculate the excess noise factor of the PP.

C.4 Ratio of the Quantum Efficiencies

From the prior analysis in chapter 6, the number of photoelectrons from each phototube can be found. Seen in figure C.1 are the number of photoelectrons for the same runs. It should be noted that the slope of this relationship is close to one, the ratio of the number of photoelectons/ being equivalent to the ratio of the quantum efficiencies (eqn. C.6).

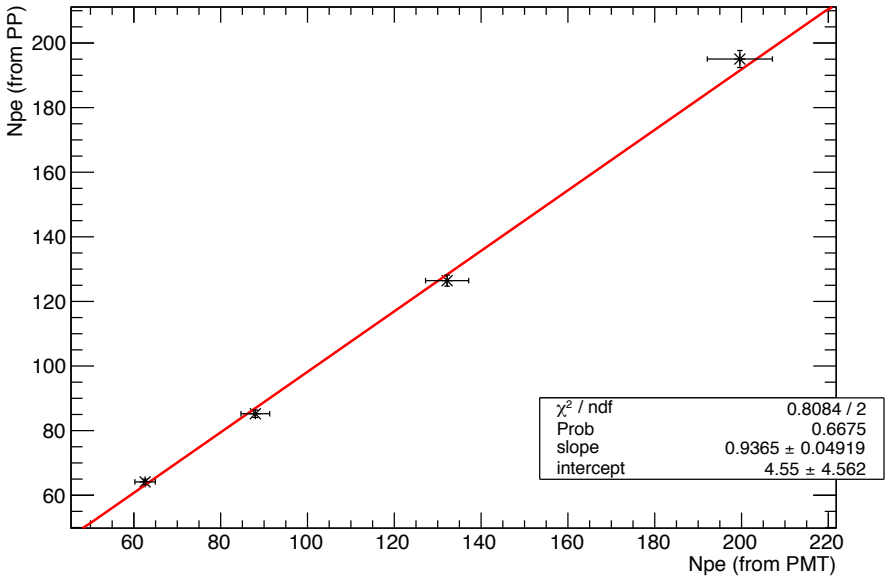

Figure C.1: *Since the number of photoelectrons can be found for both the standard PMT and the PP, their ratio should give the ratio of their quantum efficiencies. For this case, the ratio of the quantum efficiencies of the R5113-02 and the R11283 is given by the slope of the linear fit,* 0.94 ± 0.05.

Appendix D

Additional Results

D.1 Electronic Noise: Effect of Counter Timing

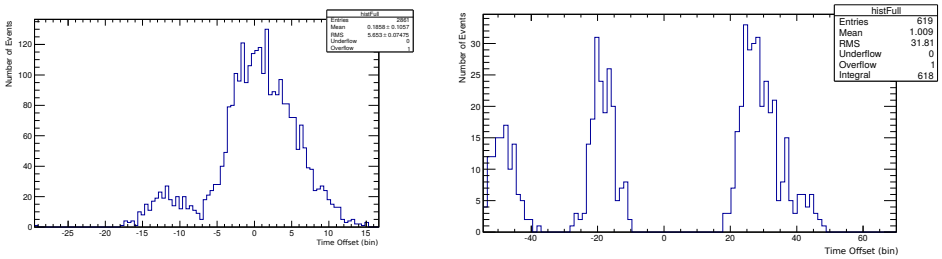

(a) *Bottom scintillator delayed.*

(b) *Top scintillator delayed.*

Figure D.1: *Time offsets for fits to the signals from the PP for different delays of the plastic scintillator counters used as the trigger. The distribution appears to be dependent on the order by which the trigger signals reach the oscilloscope.*

D.2 Residuals for Energy Linearity

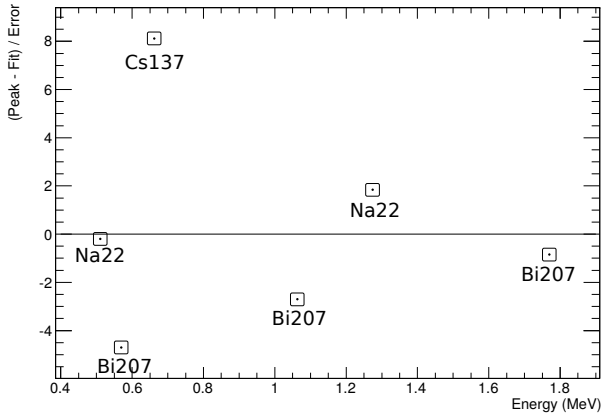

Figure D.2: *Standardized Residuals of figure 4.6. The squares are used to highlight point locations only, and are not an indication of error.*

D.3 Gain as a Function of Operating Voltage

Pictured below are the gains measured by Hamamatsu as a function of operating voltage. In figure D.3, are the gains with linear fits, and in figure D.4 is a histogram of the slopes of these fits.

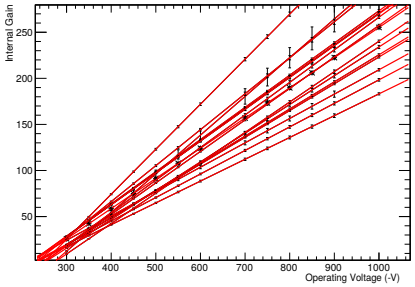

Figure D.3: *Gain as a function of the PP operating voltage for all 16 PP. Note that the gains appear to converge around* -300 *V.*

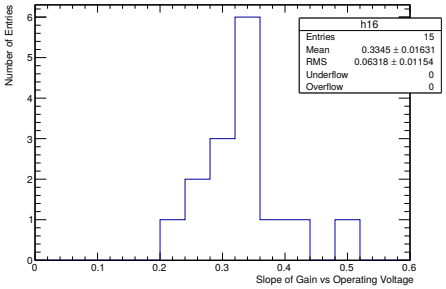

Figure D.4: *The distribution of the slopes from figure D.3. The average rate of gain increase is* $(0.335 \pm 0.016)\ V^{-1}$.

D.4 Calibration Pulse Results in Alternate Units

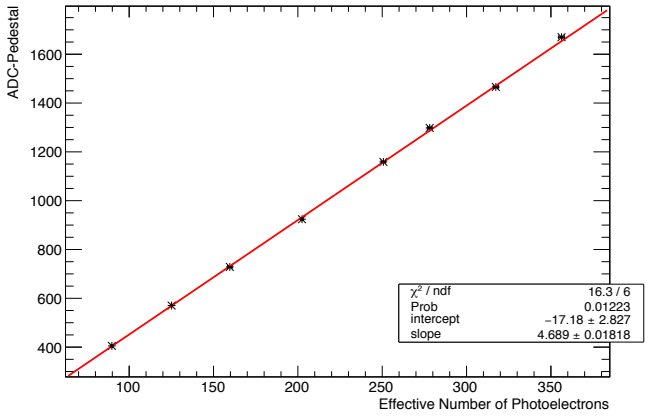

Figure D.5: *Calibration pulse test results of V3 preamp, as reported in section 6.3.4. The PP here was assumed to have a gain of 250, which is roughly the average PP gain at* -1000 *V.*

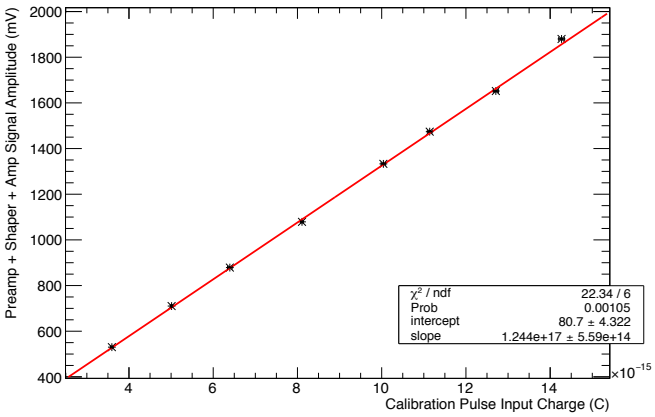

Figure D.6: *Calibration pulse test results of V3 preamp, as reported in section 6.3.4.*

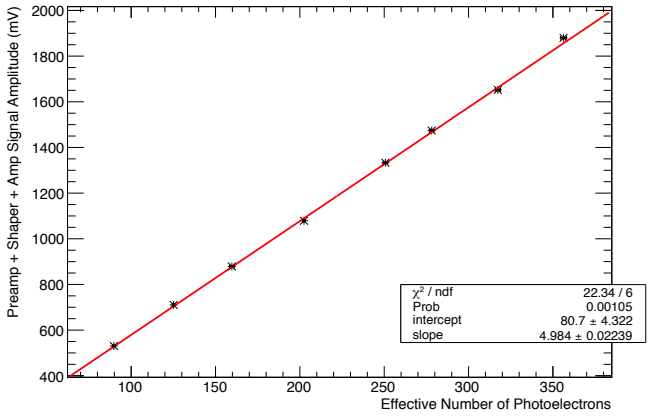

Figure D.7: *Calibration pulse test results of V3 preamp, as reported in section 6.3.4.*

D.5 Justification of Novosibirsk Use in Excess Noise Factor Raw Fits

In chapter 6, the peak height spectrum was fitted with a Novosibirsk with the claim that this was because the spectrum was asymmetric. Figures D.8 and D.9 show that the Novosibirsk indeed fits the spectra better than a Gaussian. This indicates that the spectrum is indeed asymmetric.

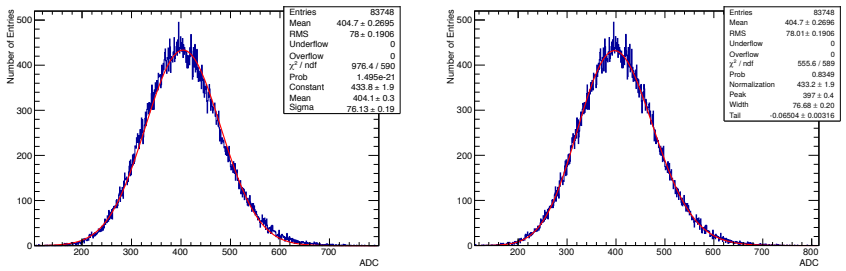

(a) *Gaussian fit.* (b) *Novosibirsk fit.*

Figure D.8: *Comparing the fits to the laser pulse spectra of chapter 6.*

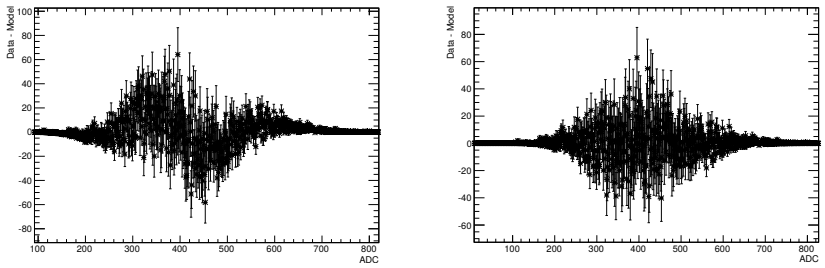

(a) *Gaussian fit residuals.* (b) *Novosibirsk fit residuals.*

Figure D.9: *Residuals of the fits in figure D.8. It is seen that the Novosibirsk function fits the data much better than the Gaussian.*

D.6 Screenshot of Calibration Pulse Signal

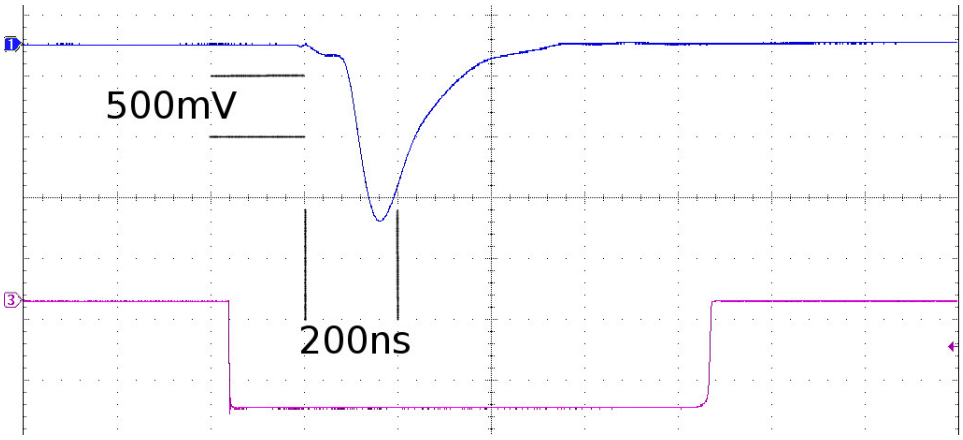

Figure D.10: *Screenshot of the average of 512 calibration pulse signals using the Tektronix oscilloscope. This signal is after the amplification and the shaping. The upper line is the signal from the preamp, while the lower line is the gate used for the ADC trigger.*

D.7 Details on the Aging Measurement

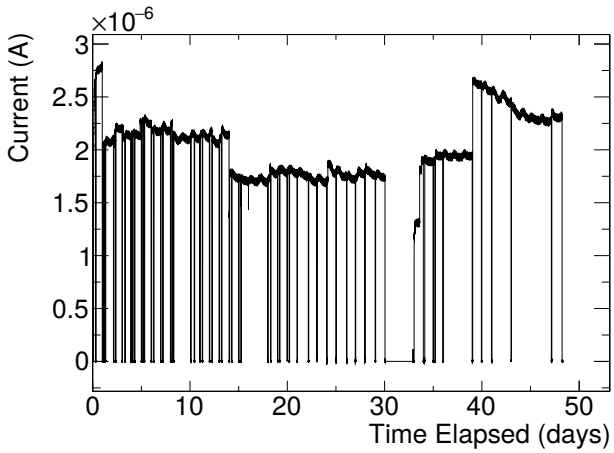

Figure D.11: *Current passing through the modified preamp as a function of time. The spikes occur when the LED is turned off to take a* ^{207}*Bi spectrum. It was observed that the current oscillated over the course of the day. This was most likely due to variations in temperature affecting the LED array, which was exterior to the incubator.*

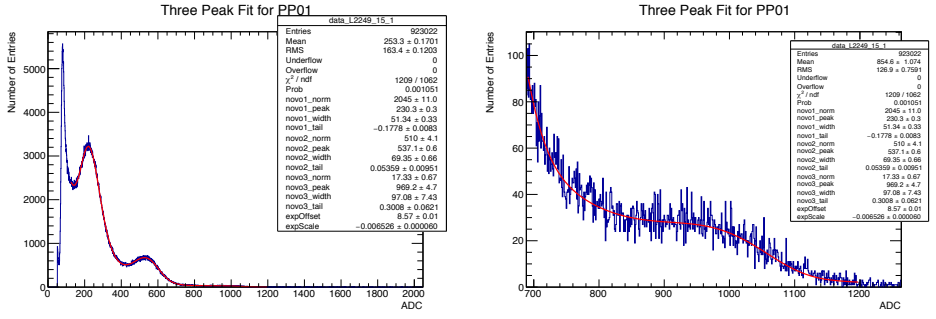

(a) *Full range.* (b) *Zoomed on 1.7 MeV peak.*

Figure D.12: *Fit to all three energy peaks of the* ^{207}*Bi spectrum with the sum of three Novosibirsk functions and an exponential.*

To group like PP together, the slopes of a linear fit to the PP performance (figs 7.10 & 7.11) before and after a given charge were compared, as seen in figure D.13. Table D.1 describes the criteria for sorting. Note that under

this scheme, the control PP was labelled as a phototube that did not age at all.

Table D.1: *Categorization outline for the PP aging, where S_b and S_a are the slopes before and after 1C respectively. The values were chosen arbitrarily to match a visual analysis of the progression of the PP performance. For the results of the categorization, refer to figure D.13.*

Colour	Attributed Significance	Requirement
Green	Aged (burned), then stopped	$S_b/S_a > 4$ and $S_a > -0.5$
Blue	Aged(burned), then slowed	$S_b/S_a > 4$ and $S_a < -0.5$
Black	Aged at a continuous rate	$S_b/S_a < 4$ and $S_a < -0.5$
Red	Didn't age at all	$S_b > 0$ or $S_a > 0$
None	Control PP	

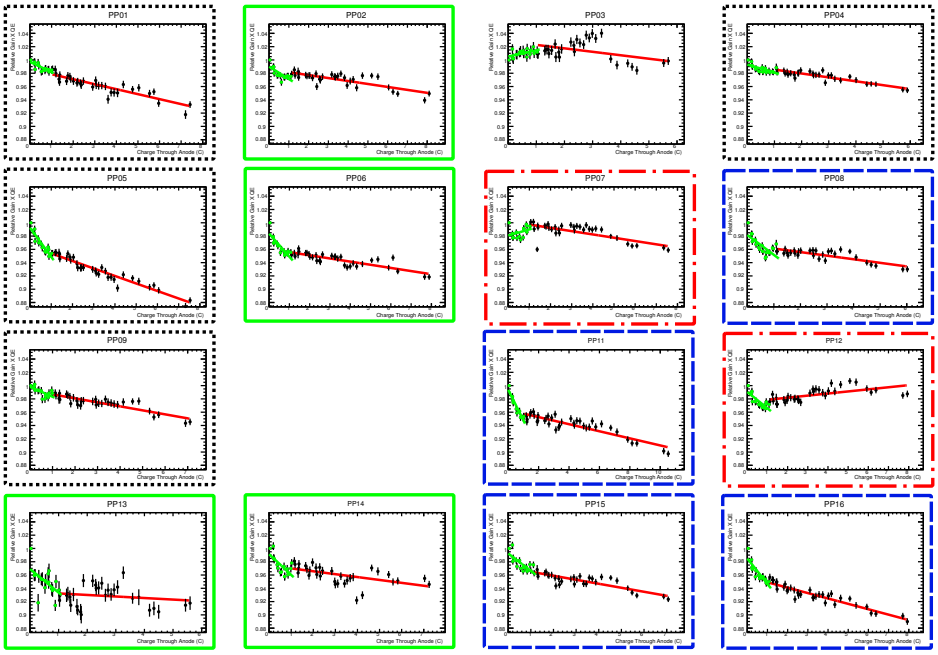

Figure D.13: *Relative PP performance with categorization, as a function of charge. The PP have been divided into four categories: aged for a period, then stopped (solid); aged, but didn't stop (– – –); aged at a constant rate throughout (· · ·); and no aging at all (– · –).*